

# **Simulation of the Sputtering of Ions from the KATRIN Main Spectrometer Surface with Geant4**

Master's Thesis of

Maximilian Beyer

at the Department of Physics  
Institute of Experimental Particle Physics (ETP)

Reviewer: Prof. Dr. Guido Drexlin  
Second reviewer: Prof. Dr. Ulrich Husemann  
Advisor: M.Sc. Dominic Hinz

31st November 2019 – 1st December 2020

Karlsruher Institut für Technologie  
Fakultät für Physik  
Postfach 6980  
76128 Karlsruhe

---

I declare that I have developed and written the enclosed thesis completely by myself, and have not used sources or means without declaration in the text.

**PLACE, DATE**

.....  
(Maximilian Beyer)



# Abstract

The story of the Karlsruhe Tritium Neutrino Experiment (KATRIN) begins with the unconventional lines "Liebe Radioaktiven Damen und Herren, [...] (ich bin) auf einem verzweifelten Ausweg verfallen um den Wechselsatz der Statistik und den Energiesatz zu retten". These words introduce the letter from W. Pauli to the *Gruppe der Radioaktiven Gauvereins-Tagung* in Tübingen in 1930 [1]. In this historical document Pauli postulated out of necessity a particle which is known today as neutrino. In the beginning, the neutrino corresponded to a hypothesis, but it soon became clear that it really exists. The first proof was given in 1956 in the Cowan and Reines experiment [2]. The first experimental milestone in neutrino research was created. And more were to follow. So is the proof of all three flavour types. The Standard Model was confirmed in an exemplary manner. However, towards the end of the twentieth century, it quickly became clear that neutrino physics was to be equated with physics beyond the Standard Model. The proof of the neutrino oscillation in 1998 by the Super Kamiokande experiment [3] shows that neutrinos have a mass, although the Standard Model contains a mass equal to zero. The KATRIN experiment is based on this experimental finding.

The neutrino mass is the linchpin of current neutrino research. The goal of the KATRIN experiment is to measure the electron anti neutrino mass with an unprecedented accuracy of  $0.2 \text{ eV}/c^2$  [4]. The basis is the energy spectrum of the tritium  $\beta$  decay, which, depending on the square of the neutrino mass, undergoes a slight shift towards low energies. Since the magnitude of the shift is in the sub-eV range, a high level of statistics is required to prove this experimental. Two central components of the experiment are decisive for this. The first is the windowless gaseous tritium source (WGTS), which guarantees a stable high luminosity and the MAC-E filter principle, which allows an excellent energy resolution. Depending on the electromagnetic configuration of the main spectrometer the background exceeds the design value by a factor of 20-50 [5]. It is precisely to this problem that the present thesis is attached.

A milestone in KATRIN's background reduction was reached with the installation of the copper baffles. This has reduced the background caused by Radon by 95% [6]. This success allows a more detailed characterisation of the remaining background. The dependence of the background on pressure, B-field setting, voltage of the inner electrodes and spectrometer temperature was investigated. The central finding is that the desired generation mechanism must produce low energy electrons homogeneously in the spectrometer. This leads to the concept of the Rydberg background model. Rydberg atoms are electrically neutral highly excited atomic states. A potential creation mechanism of these electrically neutral, highly excited states is related to sputtering due to fast ions after radioactive decays. Further measurements have shown that a  $^{210}\text{Pb}$  activity is detectable inside KATRIN. This is due to a  $^{222}\text{Rn}$  contamination of the inner main spectrometer wall during

---

the installation of the inner electrode. Thus it is shown that sputtering can be part of the underlying background generation mechanism. The focus of this thesis is on the effect of sputtering on the KATRIN background.

In sputtering, predominantly neutral atoms are released from the solid structure some of which in excited states. The probability of a high level of excitation decreases with  $n^{-3}$  [7]. However, since high excitation is associated with a long lifetime and thus the homogeneity condition of the background, a large proportion of the sputtered particles cannot fulfil the homogeneity condition. A small part of the sputtered particles is electrically charged. Due to the existing E-fields, these particles experience an acceleration and can therefore fulfil the homogeneity condition even at low excitation energies if they neutralise themselves by electron capture. In order to estimate the effect of the sputtered ions on the background, a sputtering simulation has been created using the Geant4 framework. The physics underlying the simulation is based on shielded Coulomb interactions on an atomic basis. For realistic initial conditions, the simulation starts with the implantation of the radioactive particles into the spectrometer wall and thus with the decay of  $^{222}\text{Rn}$ . The actual sputtering analysis begins with the decay of  $^{210}\text{Pb}$ . In the context of the KATRIN experiment SRIM sputtering analyses have been performed in the past [7, 8]. Serving as a benchmark, SRIM results of the basic quantities such as implantation depth and angular distribution have been compared with this work and are classified as compatible. The estimation based on the simulation to evaluate the effect of sputtered ions results in a negligible effect on the background. This is mainly due to the generally low electron density near the spectrometer wall. This results in a very small probability of ion neutralisation. Therefore, the main result of this work is that sputtered ions do not play a significant role in the remaining background signal.

The work concludes with the investigation of the impact of tritium contamination in winter 2019/2020. The focus is on the description of the contamination process in the context of basic vacuum physics. The underlying data analysis differentiates between individual detector rings and thus provides insight into the temporal background dynamics of individual flux tube volume areas.

# Zusammenfassung

Die Geschichte des Karlsruher Tritium Neutrino Experiments (KATRIN) beginnt mit den unkonventionellen Zeilen "Liebe Radioaktiven Damen und Herren, [...] (ich bin) auf einem verzweifelten Ausweg verfallen um den Wechselsatz der Statistik und den Energiesatz zu retten". Diese Worte leiten den Brief von W. Pauli an die *Gruppe der Radioaktiven Gauvereins-Tagung* zu Tübingen im Jahr 1930 ein [1]. In diesem historischen Schriftstück postulierte Pauli aus der Not heraus ein Teilchen, welches heute unter dem Namen Neutrino bekannt ist. Zu Beginn entsprach das Neutrino einer Hypothese, jedoch wurde schnell klar, es existiert wirklich. Der erste Nachweis erfolgte 1956 im Cowan und Reines Experiment [2]. Der erste experimentelle Meilenstein der Neutrinoforschung ward geschaffen. Und weitere sollten folgen. So gelang zum Beispiel der Nachweis aller drei Flavour Arten. Dies bestätigte das Standardmodell in vorbildlicher Weise. Jedoch wurde gegen Ende des zwanzigsten Jahrhundert schnell klar, dass Neutrinophysik an Physik jenseits des Standardmodell gekoppelt ist. Der Nachweis der Neutrinooszillation im Jahr 1998 durch das Super-Kamiokande-Experiment [3] zeigte, dass Neutrinos eine Masse haben, anders als im Standardmodell vorhergesehen. Auf dieser experimentellen Erkenntnis basiert das KATRIN Experiment.

Die Neutrinomasse ist Dreh- und Angelpunkt aktueller Neutrinoforschung. Das Ziel des KATRIN Experiments ist mit nie zuvor dagewesener Genauigkeit von  $0,2 \text{ eV}/c^2$  die Elektroantineutrinomasse zu vermessen [4]. Grundlage bildet das Energiespektrum des Tritium  $\beta$ -Zerfalls, welches in Abhängigkeit des Neutrinomassenquadrats eine leichte Verschiebung hin zu geringen Energien erfährt. Da die Größenordnung der Verschiebung im sub-eV Bereich ist, ist eine hohe Statistik nötig, um diese experimentell nachzuweisen. Hierfür sind zwei zentrale Bauteile des Experiments entscheidend. Zum einem die fensterlose gasförmige Tritiumquelle (WGTS), welche eine stabil hohe Luminosität garantiert und das MAC-E Filter Prinzip, welches eine hervorragende Energieauflösung möglich macht. Abhängig von der elektromagnetischen Konfiguration des Hauptspektrometers übersteigt der Untergrund den Designwert um einen Faktor von 20-50 [5]. Genau an dieses Problem knüpft die vorliegende Arbeit an.

Ein Meilenstein bei der KATRIN Untergrundreduzierung konnte mit der Installation der Kupfer Baffles erreicht werden. Hierdurch ist der durch Randon verursachte Untergrund um 95% gesunken [6]. Dieser Erfolg ermöglicht eine nähere Charakterisierung des restlichen Untergrundes. So ist die Abhängigkeit des Untergrunds vom Druck, B-Feld Einstellung, Spannung der inneren Elektroden und der Spektrometertemperatur untersucht worden. Die zentrale Erkenntnis ist, dass der gesuchte Erzeugungsmechanismus niederenergetische Elektronen homogen im Spektrometer erzeugen muss. Dies führt zur Überlegung des Rydberguntergrundmodells. Rydbergatome sind elektrisch neutrale, hoch angeregte atomare Zustände. In diesem Zusammenhang bedingt elektrisch neutral eine homogene Verteilung

---

im Hauptspektrometer und hoch angeregte Zustände können eine Quelle niederenergetischer Elektronen sein. Als mögliche Ursache gilt Sputtering aufgrund von radioaktiven Zerfällen. Weitere Messungen haben ergeben, dass eine  $^{210}\text{Pb}$  Aktivität im Inneren von KATRIN nachweisbar ist. Diese ist auf eine  $^{222}\text{Rn}$  Kontamination der inneren Hauptspektrometerwand beim Aufbau der inneren Elektrode zurückzuführen. Somit ist gezeigt, dass Sputtering teil des Untergrunderzeugungsmechanismus sein kann. Die Arbeit fokussiert sich auf die Frage nach der Auswirkung des Sputterings auf den KATRIN Untergrund.

Beim Sputtering werden überwiegend neutrale Atome in einem angeregten Zustand aus der Festkörperstruktur herausgelöst. Die Wahrscheinlichkeit der Höhe der Anregung nimmt mit  $n^{-3}$  ab [7]. Da jedoch eine hohe Anregung mit hoher Lebenszeit und damit der Homogenitätsbedingung des Untergrund einhergeht, kann ein Großteil der gesputterten Teilchen die Homogenitätsbedingung nicht erfüllen. Ein kleiner Teil der gesputterten Teilchen ist elektrisch geladen. Diese erfahren aufgrund der vorhandenen E-Felder eine Beschleunigung und können somit auch bei kleinen Anregungsenergien die Homogenitätsbedingung erfüllen, wenn sie sich durch Elektroneneinfang neutralisieren. Um die Auswirkung der gesputterten Ionen auf den Untergrund abzuschätzen ist mit Hilfe des Geant4 Framework im Rahmen dieser Arbeit eine Sputtering Simulation erstellt worden. Die der Simulation zugrunde liegende Physik basiert auf abgeschirmter Coulomb Wechselwirkung auf atomarer Basis. Für realistische Anfangsbedingungen beginnt die Simulation bei der Implantation der radioaktiven Teilchen in die Spektrometerwand und somit beim Zerfall von  $^{222}\text{Rn}$ . Die eigentliche Sputteringanalyse beginnt mit dem Zerfall von  $^{210}\text{Pb}$ . Im Kontext des KATRIN Experiments sind in der Vergangenheit SRIM Sputteringanalysen durchgeführt worden [7, 8]. Als Maßstab dienend, sind SRIM Ergebnisse der grundlegenden Größen wie Implantationstiefe und Winkelverteilung mit dieser Arbeit verglichen worden und als kompatibel eingestuft. Die auf der Simulation basierenden Abschätzung zur Bewertung der Auswirkung von gesputterten Ionen ergibt eine vernachlässigbar kleine Wirkung auf den Untergrund. Grund hierfür ist insbesondere die allgemein geringe Elektronendichte nahe der Spektrometerwand. Dies bedingt eine sehr kleine Wahrscheinlichkeit der Ionenneutralisierung. Somit kann als zentrales Ergebnis dieser Arbeit festgehalten werden, dass gesputterte Ionen nicht signifikant zum verbleibenden Untergrundsignal beitragen.

Die Arbeit schließt mit der Untersuchung der Auswirkung der Tritiumkontamination im Winter 2019/2020. Der Schwerpunkt liegt in der Beschreibung des Kontaminationsprozesses im Kontext grundlegender Vakuumphysik. Die dahinterliegende Datenanalyse differenziert zwischen einzelnen Detektorringen und ermöglicht somit den Einblick in die zeitliche Untergrunddynamik einzelner Flussschlauchvolumenbereiche.

# Contents

<b>Abstract</b>	<b>i</b>
<b>Zusammenfassung</b>	<b>iii</b>
<b>1. Neutrino physics</b>	<b>1</b>
1.1. History of neutrino discovery . . . . .	1
1.2. Standard model . . . . .	2
1.3. Neutrino oscillation . . . . .	4
1.4. Approaches to neutrino mass determination . . . . .	7
1.4.1. Neutrino oscillation . . . . .	7
1.4.2. Double $\beta$ decay . . . . .	7
1.4.3. Cosmological observations . . . . .	8
1.4.4. Direct measurement . . . . .	9
<b>2. KATRIN Experiment</b>	<b>11</b>
2.1. Tritium-Decay . . . . .	11
2.2. Main components . . . . .	12
2.2.1. Tritium source . . . . .	13
2.2.2. Transport system . . . . .	13
2.2.3. Spectrometers . . . . .	14
2.2.4. Detector . . . . .	16
2.3. Background in the Main Spectrometer . . . . .	17
2.3.1. Radon . . . . .	18
2.3.2. Motivation of Rydberg model . . . . .	20
2.3.3. Rydberg model . . . . .	25
2.4. Sputtering . . . . .	27
<b>3. Methods of Geant4-based simulations</b>	<b>31</b>
3.1. General programme flow and Mandatory classes . . . . .	31
3.2. Simulation setup . . . . .	33
<b>4. Sputtering simulation via Geant4</b>	<b>37</b>
4.1. Implantation . . . . .	37
4.2. Decay Chain . . . . .	39
4.3. $^{210}\text{Pb}$ Decay . . . . .	41
4.4. Impact of sputtering . . . . .	44
<b>5. Tritium analysis</b>	<b>49</b>

<b>6. Conclusion</b>	<b>53</b>
<b>Bibliography</b>	<b>55</b>
<b>A. Appendix</b>	<b>61</b>
A.1. Stainless steel composition in Geant4 . . . . .	61
A.2. Penetration depth and variance along the decay chain . . . . .	62
A.3. Sputtering Simulation results . . . . .	62
A.4. Excluded pixels and run numbers . . . . .	65
A.5. Background rates over time per ring . . . . .	67

# List of Figures

1.1.	Cowan and Reines . . . . .	2
1.2.	Standard Model . . . . .	3
1.3.	Result plots for SNO and Super Kamiokande . . . . .	6
1.4.	KamLand neutrino oscillation . . . . .	8
1.5.	Neutrinoless $\beta$ decay and sketch of GERDA experiment . . . . .	8
2.1.	Beamline KATRIN . . . . .	11
2.2.	Tritium energy spectrum of the $\beta$ electrons and schematic diagram of the $\beta$ decay . . . . .	12
2.3.	Sketch WGTS . . . . .	13
2.4.	Sketch of the differential pumping system . . . . .	14
2.5.	MAC-E Filter principle . . . . .	16
2.6.	Detector Resolution . . . . .	17
2.7.	Effect of the copper baffles . . . . .	19
2.8.	Uranium Radium decay chain . . . . .	21
2.9.	Radial distribution background rate and Poisson distributed background . . . . .	22
2.10.	Background reduction baking and B-Field variation . . . . .	22
2.11.	Background pressure dependence . . . . .	24
2.12.	Background voltage dependence . . . . .	24
2.13.	BBR and Rydberg energy states . . . . .	25
2.14.	Field ionisation and background temperate dependency . . . . .	26
2.15.	Sputtering in context of KATRIN . . . . .	27
3.1.	Code example Geant4 . . . . .	32
3.2.	Surface profile in Geant4 simulation . . . . .	34
3.3.	Sketch of classical Scattering Problem . . . . .	36
4.1.	Range of $^{218}\text{Po}$ recoil in air . . . . .	38
4.2.	Implantation depth . . . . .	40
4.3.	Change of implantation depth . . . . .	40
4.4.	Scatter plots full decay chain . . . . .	41
4.5.	Parameter study . . . . .	42
4.6.	Implantation systematic . . . . .	43
4.7.	Theta distribution of different sputtered species . . . . .	44
4.8.	Results sputter analysis . . . . .	45
4.9.	Simulated radius distribution and energy distribution of electrons of $^{210}\text{Po}$ . . . . .	47
5.1.	Background rates over radius of analysing plane . . . . .	50
5.2.	Total background rate over time . . . . .	51

*List of Figures*

---

5.3.	Background rates over time per ring part I . . . . .	52
5.4.	Normalised total background rates over radius . . . . .	52
A.1.	Sputtering results part one . . . . .	62
A.2.	Sputtering results part two . . . . .	63
A.3.	Sputtering results part three . . . . .	63
A.4.	Sputtering results part four . . . . .	63
A.5.	Sputtering results part five . . . . .	64
A.6.	Sputtering results part six . . . . .	64
A.7.	Background rates over time per ring part II . . . . .	67
A.8.	Background rates over time per ring part III . . . . .	68
A.9.	Background rates over time per ring part IV . . . . .	69

# List of Tables

3.1. Mandatory and optional user classes for Geant4 . . . . .	32
A.1. Penetration depth . . . . .	62
A.2. Excluded detector pixel . . . . .	65
A.3. List one of run numbers . . . . .	65
A.4. List two of run numbers . . . . .	66



# 1. Neutrino physics

It has already been 90 years now that the neutrino was postulated by Wolfgang Pauli [1]. With the help of the new, light and electrically neutral elementary particle, the continuous  $\beta$  decay spectrum can be explained. This opened a new chapter in particle physics. The search for an almost undetectable particle has begun.

Chapter 1.1 summarises the history of neutrino discovery by means of central experiments. Chapter 1.3 deals with the neutrino oscillation. Basic experimental and theoretical considerations are presented. A classification into the Standard Model is given in chapter 1.2. The last chapter gives an overview of different approaches to determine the neutrino mass.

## 1.1. History of neutrino discovery

In  $\beta^-$  decay a neutron is transformed into a proton, electron and electron-antineutrino. The existence of the electron-antineutrino was not known to anyone at the beginning of the 20th century. Therefore it is surprising that the energy spectrum of the  $\beta$  decay is continuous. In conformity with energy and momentum conservation, a discrete spectrum according to

$$\frac{E_1}{E_2} = \frac{m_2}{m_1} \quad (1.1)$$

can be expected for the two-body decay. To solve this discrepancy Pauli postulated a new elementary particle in 1930, which is known today as Neutrino [1]. The experimenters of that time were long faced with the challenge of detecting a particle with only weak interaction. In 1956, the Cowan and Reines experiment at the Savannah River Reactor succeeded in doing so, see figure 1.1. The detection method of the experiment was based on the inverse  $\beta$  decay, see equation 1.2. The underground experimental setup consists of two water tanks with a total volume of 200 liters, 10 meters away from the reactor core. In addition to water, the tank contains 40 kilograms of cadmium chloride. Scintillators for photon detection are installed around the tank. [2]



The resulting positron from the inverse  $\beta$  decay is annihilated with one electron, resulting in two  $\gamma$  quanta with 511 keV energy each. After thermalization, the neutron binds with the cadmium chloride in the tank, also generating one  $\gamma$  quantum. By a delayed coincidence measurement of a positron and neutron signals, a neutrino detection is possible. In 1995, the first experimental detection of neutrinos was awarded the Nobel Prize in Physics.



Figure 1.1.: Neutrino pioneers at work. Cowan is on the left and Reines on the right. The project team has called the project Poltergeist.[9]

In addition to the electron neutrino, there are also the muon neutrino and tau neutrino. The detection of these two neutrino flavors follow the same generalised production mechanism as for the electron neutrino

$$\nu_l + X \rightarrow l^{+/-} + Y. \quad (1.3)$$

Here X and Y stand for hadronic states and l for charged leptonic states. Despite the same production mechanism, the detection of muon and tau neutrino is much more difficult. The muon neutrino was detected in 1962 at the proton accelerator in Brookhaven. Collisions of high-energy protons with the beryllium target produce charged  $\pi$  mesons. These decay into muons and muon neutrinos. Only the neutrinos are able to pass through the 5000 ton steel absorber and generate a signal at the detector. In 1988 this discovery was awarded with a Nobel Prize.[10]

The detection of the tau neutrino was successful in 2001 at the DONUT detector in the FermiLab [11]. The short lifetime of the tau leptons poses a great experimental challenge, hence the late detection. [10]

## 1.2. Standard model

The Standard Model [12] (SM) of particle physics is a comprehensive theory for describing fundamental elementary particles and their interactions in the context of electromagnetic, weak and strong interaction. Gravitation is not included in the Standard Model. In SM, the different elementary particles are divided into different categories. As shown in figure 1.2 there are leptons, quarks, vectorial and scalar gauge bosons. The bosons are carriers of the

interactions, whereas the fermions are the basis of matter. In this context every element can be sorted like for example tritium. Tritium consists of one proton, two neutrons and one electron. The proton itself is composed of two u-quarks and a d-quark, while the neutron is composed of two d-quarks and a u-quark. So tritium can be described as a fermion combination of four u- and five d-quarks and one electron. For a complete description of tritium, the gauge bosons must also be taken into account. The gluons are the carriers of the strong interaction that enables the formation of the atomic nucleus. Photons as electromagnetic exchange particles determine the chemical properties of tritium. The vector bosons of the weak interaction enable the  $\beta$  decay. The Higgs boson, which has been omitted so far, gives each particle its mass.

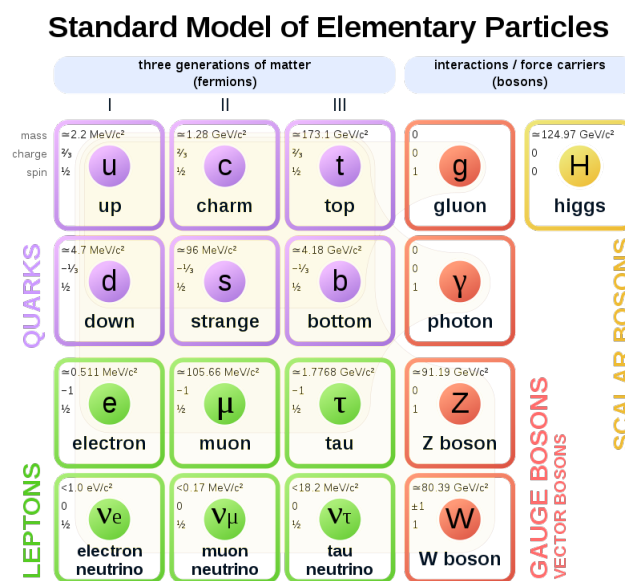


Figure 1.2.: Standard Model of particle physics. The fundamental structure of matter and its non-gravitational interactions can be explained with the help of 61 elementary particles. This count includes antiparticles and all colour charge combinations. [13]

Although the Standard Model explains large parts of the world accessible to us, some issues are not included in SM. As already mentioned, any effect of gravity is missing. Furthermore, there is no particle candidate in SM that can explain dark matter. Depending on the model, dark matter accounts for 24.4% of the total energy density of the universe [14]. From a physical point of view unsatisfactory, but not necessarily wrong, is the high number 26 of degrees of freedom and therefore experimentally determinable parameters of the SM. In the context of this work it is particularly interesting that the SM does not provide mass for neutrinos. As shown in chapter 1.3, this assumption is not tenable. In the context of SM, the KATRIN experiment is in the study of physics beyond the Standard Model. Specifically, the free parameter of the electron neutrino mass will be determined experimentally.

### 1.3. Neutrino oscillation

Neutrino oscillation describes the periodic flavour conversion of neutrinos. Due to this process, the probability of observing a certain flavour state depends, among other things, on the distance to the neutrino source. The Homestake experiment [15] provides first indications for such behaviour. The breakthrough evidence is provided by the Super Kamiokande experiment [3] and the SNO (Sudbury Neutrino Observatory) experiment [16].

In the US American Homestake Mine, the homonymous Homestake Experiment started in 1967. The goal is to find proof that the sun generates its energy by nuclear fusion. For this purpose, the solar neutrinos are to be detected by radiochemical methods. A  $6 \cdot 10^5$  liter tank with tetrachloroethylene serves as target. The neutrinos interact with the chlorine and produce radioactive argon according to equation [15]



At regular intervals the argon is extracted and the decay is detected in proportional chambers. On average a reaction occurs every two days. With this experiment solar neutrinos have been detected for the first time. However, the measured rate is about one third lower than expected [17]. Besides systematic errors in the experiment or a wrong solar model, the neutrino oscillation can also explain the missing fraction of electron neutrinos. 31 years later, the last assumption turns out to be correct [16].

The big disadvantage of the homestake experiment is that it is a counting experiment. If the neutrinos exceed the energy threshold necessary for the chlorine conversion, a count occurs. The energy and directional information are lost. The Kamiokande experiment [18] in Japan overcomes this design deficit. The basic principle of measurement is not a radiochemical reaction but elastic scattering of the neutrinos with the electrons of the target material



A total of 3k tons of water as target material are contained in a cylindrical vessel which is covered with photomultipliers. Thus it is possible to detect the Cherenkov light of the recoil electrons. From the intensity of the Cherenkov rings the electron energy can be determined. In addition, the direction of movement of the electrons and their point of origin can be reconstructed from the position of the rings. [10]

This information allows two observations. First, in the direction of the sun there is a significant event rate peak. And second, the detection rate without the existence of neutrino oscillation is 50% lower than expected. [3]

The first observation clearly verifies the Sun as a neutrino source. The reduced detection rate of the second observation is a further indication of the neutrino oscillation. Although muons and tau neutrinos are also involved in the underlying elastic scattering, the effective cross section for this flavor is suppressed by a factor of about five in the sensitive energy range. This suppression is due to the fact that only the charged current (cc) channel is available, while electron neutrinos also act via neutral current (nc) channel. Therefore, a

lower rate can be expected in the case of an existing neutrino oscillation.

The upgraded Super Kamiokande experiment is similar to its predecessor, but with 50k tons of water it has a multiple of the detector mass. Due to the increased sensitivity, it was possible to detect neutrino oscillation for the first time with this setup. The observed neutrinos are the interaction product of the cosmic rays with the atmosphere, therefore they are atmospheric neutrinos. [19]

The breakthrough in the detection of solar neutrino oscillation was achieved with the SNO experiment [16]. The experiment is set up in the Sudbury Mine in Canada. It consists of a 12 m diameter sphere with 1k ton of heavy water. The outer volume contains ultra pure water, which serves as a shield. The entire structure is surrounded by 9456 PMT. The conceptual advantage of the SNO experiment is that the solar neutrinos are measured on three different reaction channels. On the one hand, the cc channel of the electron neutrinos with



is available.

Furthermore, all three flavours can interact with deuterium via nc-interaction



Finally, as in the Kamiokande experiment, the elastic scattering according to equation 1.5 is detectable.

The combination of the three detection pathways shows that the total neutrino flux is composed of the three flavours and corresponds to the theoretically expected flux. Thus, there is no neutrino loss, but a flavour conversion described by the neutrino oscillation. The result is summarized in figure 1.3. The three colored bands correspond to the three detection channels. Blue is the total flux from the nc channel, therefore the sum of x and y is always constant in the blue area. The red band is the cc channel on which only the electron neutrinos are sensitive, therefore the slope is infinite. The green band describes the elastic scattering. The high slope is due to the fact that the cross section of the electron neutrinos in the sensitive range is larger by a factor of five to six compared to the others. [16]

The discovery of the neutrino oscillation was honoured with the Nobel Prize in 2015 to A. McDonald and T. Kajita, the directors of the experiments [20].

In the following, the neutrino oscillation is described in mathematical form. The basic idea is that the flavoure eigenstate does not equal to the mass eigenstate. Therefore the state which determines the interaction is different from the propagation term. This allows a transformation of the flavour during propagation. Although it is a quantum mechanical interference effect, this phenomenon can be observed in macroscopic space.

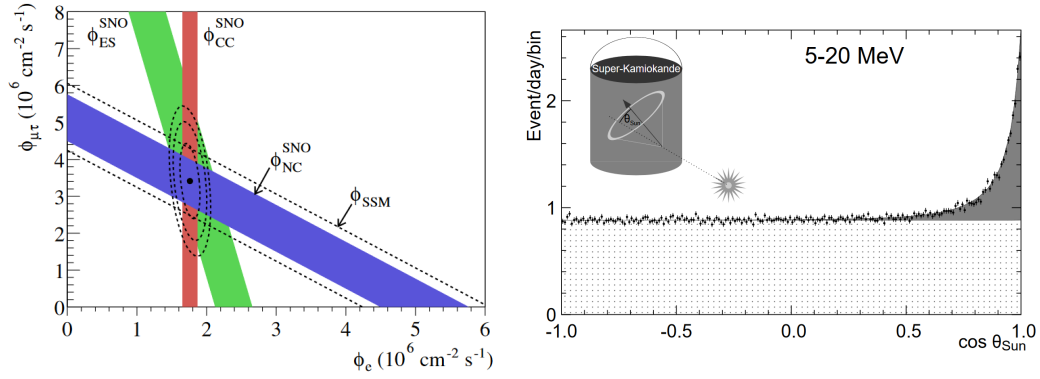


Figure 1.3.: Left: Result plot of the SNO experiment. On the x-axis the electron neutrino flux is plotted and on the y-axis the muon and tau neutrino flux. The three differently colored bands correspond to the three measuring channels of the experiment, see text. [16] Right: Plot from the Super Kamiokande experiment. The event rate is plotted over angle to the sun. There is a significant peak in the direction of the sun. [3]

The basis of the description is the neutrino mixing matrix (PMNS<sup>1</sup>), see equation 1.8.

$$\begin{bmatrix} \nu_e \\ \nu_\mu \\ \nu_\tau \end{bmatrix} = \begin{bmatrix} U_{e1} & U_{e2} & U_{e3} \\ U_{\mu1} & U_{\mu2} & U_{\mu3} \\ U_{\tau1} & U_{\tau2} & U_{\tau3} \end{bmatrix} \begin{bmatrix} \nu_1 \\ \nu_2 \\ \nu_3 \end{bmatrix} \quad (1.8)$$

Here  $\nu_\alpha$  with  $\alpha = (e, \mu, \tau)$  describes the flavour eigenstates and  $\nu_i$  with  $i = (1, 2, 3)$  the mass eigenstates. The wave function of any neutrino flavour is

$$\Psi(x, t) = \sum_i U_{\alpha i} e^{E_i t - p x} \nu_i. \quad (1.9)$$

In this equation, mass eigenstates can be replaced by flavour eigenstates, whereby it should be noted that the mixture matrix  $U$  is a unitary matrix. It results with

$$\vec{\nu}_i = U_{\beta i}^+ \vec{\nu}_\beta \quad (1.10)$$

following term

$$\Psi(x, t) = \sum_\beta A_{\alpha\beta}(x, t) \nu_\beta. \quad (1.11)$$

$A_{\alpha\beta}$  represents the probability amplitude to observe the original  $\alpha$  neutrino in the  $\beta$  state. The probability is obtained by forming the square of the magnitude

$$P_{\alpha\beta}(x, t) = |A_{\alpha\beta}(x, t) \nu_\beta|^2 = \left| \sum_i U_{\alpha i} U_{i\beta}^* e^{-i(m_i^2 t / 2p)} \right|^2. \quad (1.12)$$

<sup>1</sup>Pontecorvo–Maki–Nakagawa–Sakata

By consistently multiplying out and using the Euler identity the term can be transformed into

$$P_{\alpha\beta}(x, t) = \left| \sum_i |U_{\beta i}^*|^2 |U_{i\alpha}|^2 + 2 \sum_{i>j} |U_{\beta i}^* U_{\alpha i} U_{\beta j} U_{\alpha j}^*| \cos\left(2\pi \frac{x}{L_{ij}}\right) \right| \quad (1.13)$$

with

$$L_{ij} = 2\pi \frac{2p}{m_i^2 - m_j^2}. \quad (1.14)$$

As a result, the oscillation length  $L$  depends on the difference between the square of mass and energy. Experimentally it is advantageous to choose energies and distances in such a way that only two flavors are dominant. [12]

## 1.4. Approaches to neutrino mass determination

There are several possibilities to determine the neutrino mass or at least to restrict it in an interval. This subchapter deals with four popular experimental approaches.

### 1.4.1. Neutrino oscillation

As can be seen from formula 1.3, the oscillation length depends on the difference of the different neutrino masses to the square. From the measurement of the oscillation length, a lower limit of  $0.05 \text{ eV}/c^2$  can be determined. [21]

Figure 1.4 shows the results of the KamLAND experiment [22]. The data points correspond to the background reduced electron antineutrino flux, which is plotted over  $L_0/E$ . Here  $L_0$  corresponds to an effective baseline of 180 km. The probability of observation an electron antineutrino fluctuates periodically, as can be expected according to the formula 1.3. The deviation of an ideal periodic sine oscillation is due to the fact that several baselines are superimposed. It is easy to see that theoretical model expectation and real data are in agreement. [23]

### 1.4.2. Double $\beta$ decay

According to SM the double  $\beta$  decay is an allowed but an extremely rare decay event. It can be distinguished between the normal and the neutrinoless  $\beta$  decay. In the normal  $\beta$  decay two neutrons are transformed into two protons, two electrons and two neutrinos. In the neutrinoless variant, the same happens, but the two neutrinos annihilate directly with each other, as can be seen in the Feynman diagram in figure 1.5. The basic prerequisite for this annihilation process is that neutrinos have a mass for helicity reasons and are their own antiparticles. The first condition can be regarded as fulfilled due to the neutrino oscillation, while the second condition presupposes the majorana nature of the neutrinos. It is uncertain whether neutrinos are majorana fermions or, Dirac fermions. The observation of a neutrinoless  $\beta$  decay would provide clarity.

The GERDA experiment [24], see figure 1.5, is one of many experiments that attempts to

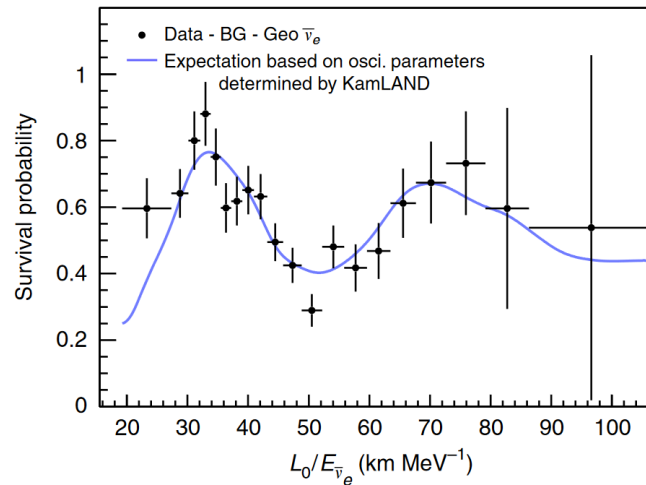


Figure 1.4.: Results KamLAND neutrino oscillation. Theoretical model expectation and real data agree. For further details see text. [23]

detect the neutrinoless  $\beta$  decay. To date, no experiment has been able to measure a signal. In the case of detection, the estimated decay rate can be used to determine the absolute mass of neutrinos. The limits for majorna neutrinos are  $(0.12 - 0.26) \text{ eV}/c^2$  (90%C.L.) [24].

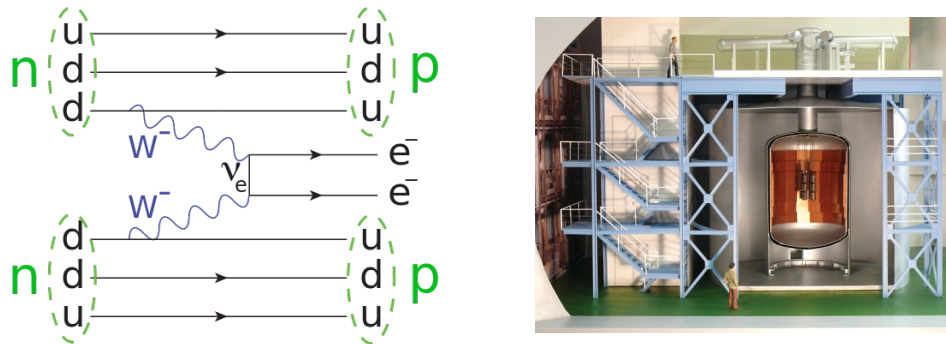


Figure 1.5.: Left: Feynman diagram of the neutrinoless double  $\beta$  decay [25]. Right: Experimental setup of the GERDA experiment [26].

### 1.4.3. Cosmological observations

Limit values can also be derived from cosmological observations. For example, an upper limit of the electron neutrino mass with  $5.7 \text{ eV}/c^2$  can be calculated from the measurement of the arrival times of the supernova SN1987A neutrinos [27]. The basic idea of such an analysis is that neutrinos have a mass and therefore their arrival time depends on the energy and their mass

$$m_\nu = \frac{2c\Delta t}{L} \left( \frac{1}{E_1^2} - \frac{1}{E_2^2} \right)^{-1}. \quad (1.15)$$

Another cosmological approach is the study of large-scale structures in the universe. In conjunction with the cosmic microwave background (CMB), limits for the neutrino mass can be determined within the framework of the cosmological Standard Model. It results that the upper limit of the sum over all neutrino masses is 0.23 eV (95% C.L.) [28]. However, this consideration is strongly model dependent.

#### 1.4.4. Direct measurement

One of the direct measurement method is based on the  $\beta$  decay. The basic idea is the exact measurement of the electron decay spectrum. Depending on the neutrino mass, the endpoint of the spectrum is shifted to low energies. The biggest advantage of all direct measurement approach is that no model assumptions are necessary. The whole kinematics is based on conservation of momentum and energy [5]. The two previous experiments of Katrin, Mainz and Troski, were also based on this principle. They measured an upper limit of  $m_\nu < 2.2 \text{ eV}/c^2$  at a confidence interval of 95% [29]. Currently, the KATRIN experiment yields the best upper mass limit of  $1.1 \text{ eV}/c^2$  at a confidence interval of 90% [30]. Which will be presented in particular in the following section.

An other method of direct measurement is based on electron capture (EC). The basic idea is to measure the total decay energy of the de-exciting atom. The difference between measured and expected energy can be explained by the neutrino mass. The HOLMES experiment is based on this principle and plans to use  $^{163}\text{Ho}$  to achieve a sensitivity of less than  $0.1 \text{ eV}/c^2$ . [31]



## 2. KATRIN Experiment

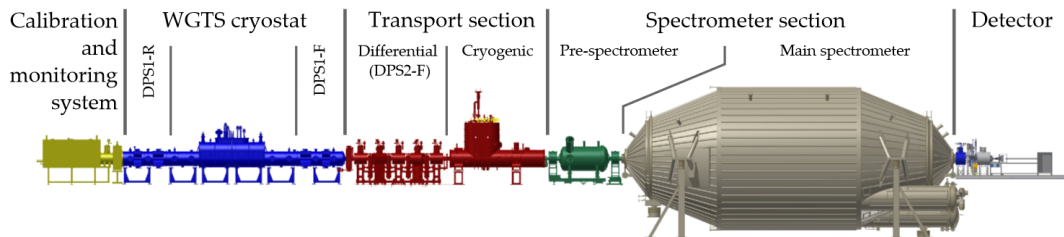


Figure 2.1.: Beamline of KATRIN. The entire KATRIN setup is about 70 m long. It starts with the Calibration and monitoring System and ends with the detector. The focus of the present thesis is on the main spectrometer section. For more details see caption 2.2. [32]

The Karlsruhe Tritium Neutrino Experiment (KATRIN) is the technical advancement of the Mainz and Troitsk neutrino experiments [33]. The goal is to determine the electron-antineutrino mass with an accuracy of  $200 \text{ meV}/c^2$ . The measurement accuracy is thus improved by one order of magnitude compared to previous experiments. The measurement principle is basically the same, because the KATRIN experiment also measures the energy spectrum of the tritium decay based on the MAC-E filter system [29].

The principle of tritium decay is presented in chapter 2.1, whereas the technical details of the experimental setup are discussed in chapter 2.2. The background noise, which is particularly important for understanding the work, is summarised in chapter 2.3. Last but not least is an introduction into the mechanics of sputtering which could be a key process to explain the main background characteristics, see chapter 2.4.

### 2.1. Tritium-Decay

Tritium ( ${}^3\text{H}$ ) is the heaviest hydrogen isotope. It consists of one proton and two neutrons. This nucleon combination is unstable and decays via a  $\beta$  decay into the stable helium-3 ( ${}^3\text{He}$ ). During the  $\beta$  decay, an electron and an electron-antineutrino are released, which are produced by the conversion of a neutron into a proton. The schematic representation of the  $\beta$  decay and the continuous energy distribution of the decay electron is shown in figure 2.2.

The goal of the KATRIN experiment is to determine the neutrino mass by precisely measuring the electron energy spectrum. This is possible due to the general conservation of energy and momentum. The decay energy of approximately 18.6 keV [34] is distributed

among electron, neutrino and recoil nucleus. This allows a random but probability distribution of energy transfer to the individual components during decay. At higher statistics the already mentioned continuous energy distribution of the electron results. At the endpoint of the spectrum, almost the entire decay energy is given to the electron. If neutrinos were massless, only a tiny part of the energy assigned to the recoil nucleus would be missing. However, since the neutrino has a mass, its generation energy must also be taken into account. Thus, the neutrino mass can be determined from the difference between the maximum decay energy and the maximum electron energy. If the neutrino mass is very small and is no longer within the range of measurement accuracy, an upper limit for the neutrino mass can still be determined.

The use of tritium offers two distinct advantages over other  $\beta$  decays. First, the endpoint energy of 18.6 keV is the second smallest of all  $\beta$  emitters. This is relevant because the probability that an electron has the energy  $E$  decreases with  $\frac{1}{E^3}$ . The second advantage of tritium is its low half-life of 12.32 years, which allows for high activity. Thus, the statistics are relatively high when measuring the end of the tritium energy spectrum.[5]

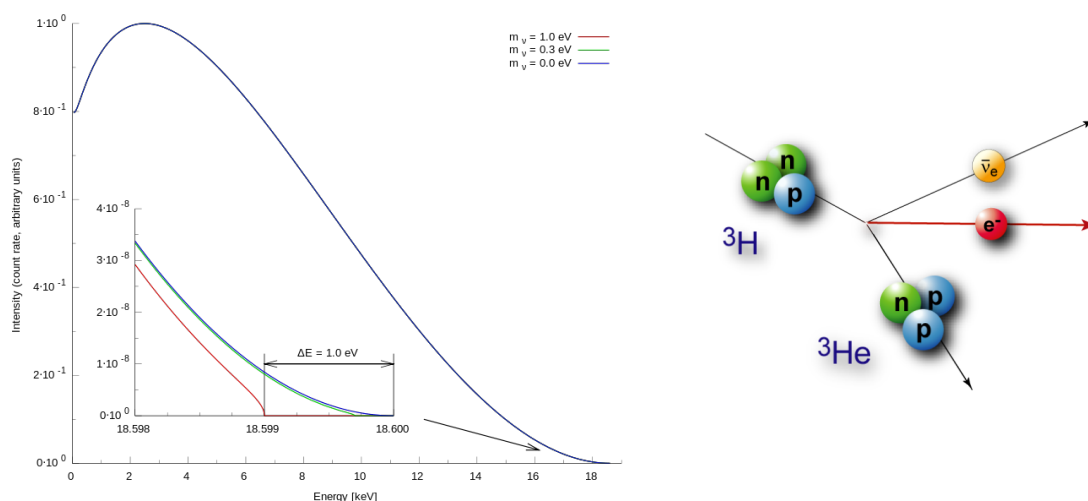


Figure 2.2.: Left: Energy spectrum of the electron with different electron-antineutrino masses. The shift of endpoint depends on electron-antineutrino masses. [35] Right: Schematic representation of the  $\beta$  decay. In the mother nucleus a neutron is transformed into a proton, electron and electron-antineutrino. The electron and electron-antineutrino leave the nucleus. [36]

## 2.2. Main components

The entire KATRIN experiment is about 70 metres long. At the beginning of the arrangement is the rear system with basic control and monitoring functions. At the end is the 65 cm<sup>2</sup> large detector, which is hit by the focused electron beam. The components in between allow selective electron focusing under strict vacuum conditions. Effectively it is possible to measure the tritium decay spectrum with an accuracy of 2.77 eV. In the

following the experimental setup is divided into four main components and described in more detail. Exact construction details can be found in [37].

### 2.2.1. Tritium source

The windowless gaseous tritium source (WGTS) provides a strongly controlled decay environment for the tritium atoms. It is a tube ten metres long and 90 mm thick in its inner diameter, in the centre of which tritium flows continuously into the inner at a pressure of  $p_{in} = 3.4 \cdot 10^{-3}$  mbar. By means of diffusion, the tritium reaches the ends of the WGTS within one second. Here are the vacuum pumps DPS1-R and DPS1-F, which reduce the tritium flow into the further parts of the experiment by a factor of  $10^2$  [6]. For ideal decay conditions, it is particularly important to note that the tritium column density of  $5 \cdot 10^{17} \frac{\#}{\text{cm}^2}$  may fluctuate by a maximum of 0.1%/h over the duration of the measurement, higher deviations lead to larger systematic errors. The selected column density is an optimisation from the desire for the highest possible source luminosity and the lowest possible scattering within the source. Furthermore, the operating temperature of the WGTS is 30 K to minimise the Doppler broadening of the electrons.[5]

The total source activity is  $10^{11}$  Bq, where the probability of a single tritium atom decaying in the source is  $10^{-9}$ . The resulting electron is guided adiabatically at a strong B-field towards the main spectrometer. In WGTS itself the B-field is 3.6 T strong. Thus the magnetic flux through the whole experiment is  $191 \text{ Tcm}^2$  [6]. [37]

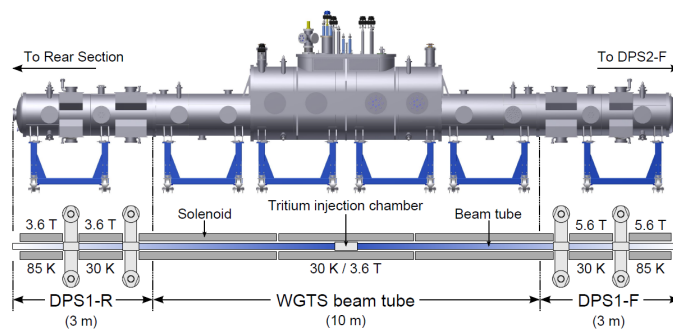


Figure 2.3.: Sketch of the WGTS. The tritium injection area is centrally located. From here the tritium diffuses to the left and right to the differential pump systems DPS1-R and DPS1-F. The density of the molecules decreases approximately linearly from the centre to the sides. The column density of tritium may only vary by 0.1%/h.[37]

### 2.2.2. Transport system

The transport system is located downstream of the WGTS. The purpose of this part of the experiment is to significantly reduce the flow of tritium from the WGTS. The degree of the necessary reduction is given by the boundary conditions that a maximum of  $10^{-3}$  tritium decays per second may take place in the main spectrometer [5]. In the case of a larger

tritium activity, the background noise would be too high. Effectively this is associated with a tritium flux reduction from source to detector by a factor of  $10^{14}$ .

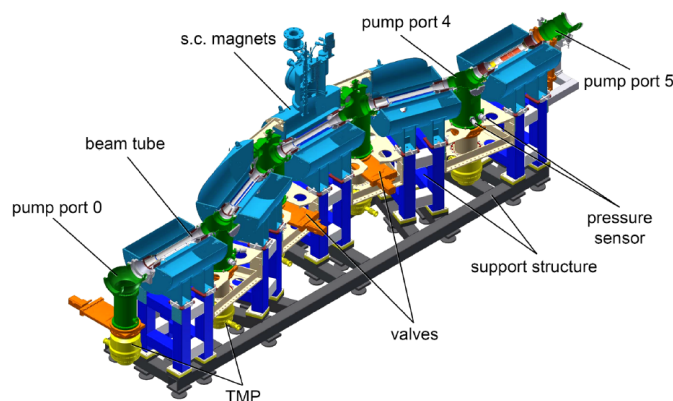


Figure 2.4.: Sketch of the differential pumping system (DPS). Four turbomolecular pumps are installed along the kinked pipe [38], which reduce the tritium flow by a factor of  $10^5$ . [37]

Experimentally, several pump systems have to be installed along the transport route to achieve the necessary reduction. In chapter 2.2.1 the DPS1-F with a reduction of  $10^2$  is presented. This is followed by the DPS2-F and CPS (Cryogenic Pumping System). In figure 2.4 the DPS2-F is shown. It consists of a pipe with four bends and four turbomolecular pumps, each of which is installed at one of the bends. Due to the curvature of the pipe, the tritium flow hits the inner wall of the pipe and is reflected. This allows an improved pumping of the  $^3\text{H}$  molecules and thus a reduction of the tritium current by a factor of  $10^5$ . A 5.6 T strong magnetic field enables the electrons to be guided through the curved tube without loss. The transport system ends with the subsequent CPS. Basic principle of the CPS is cryosorption. For this purpose, an argon frost layer is applied to the 3 K cold CPS surface, which facilitates the condensation of the tritium on the surface. The tritium flow reduction is about  $10^7$  orders of magnitude. By combining the different pumping systems, the necessary reduction of  $10^{14}$  is achieved. [37]

### 2.2.3. Spectrometers

Two spectrometers are installed in the KATRIN experiment. One is the 3.38 m long pre-spectrometer and the 23.28 m long main spectrometer [37]. Both spectrometers work like high pass filters, which are realised by the MAC-E filter system. The basic idea of the filter principle is the adiabatic guidance of the decay electrons along a B-field opposite to an E-field within the spectrometer according to figure 2.5 [39]. By a continuous decrease of the B-field towards the centre of the spectrometer, the so-called analysis plane, the part of the kinetic energy of the electrons perpendicular to the beam axis is reduced. As a result, the parallel portion increases after the energy is conserved. The reason for this connection is that due to the adiabatic movement the magnetic moment of the electrons is a constant of the movement, see equation 2.1. The basic prerequisite for this is a small gradient in

the B-field.

$$\mu = \frac{E_{\text{kin,transversal}}}{B} = \text{const.} \quad (2.1)$$

Thus the perpendicular kinetic energy component decreases towards the centre, while the parallel component increases according to 2.1. Another constant is the magnetic flux  $\Phi$ . Because of the low B-field in the middle of the spectrometer, the cross-sectional area of the flux tube must increase according to 2.2. This explains the enormous dimensions of KATRIN with an inner diameter of 9.8 m [37].

$$d_{\text{AP}} = d_S \cdot \sqrt{\frac{B_S}{B_{\text{min}}}} \quad (2.2)$$

Based on the magnetic mirrow effect  $B_S$  and  $B_{\text{min}}$  also determine the maximum acceptance angle of the spectrometer to  $51^\circ$  [37]. Electrons with too large polar angle with respect to the magnetic field will be reflected. It applies,

$$\theta_{\text{max}} = \arcsin\left(\sqrt{\frac{B_S}{B_{\text{min}}}}\right). \quad (2.3)$$

The reflection of charged particles moving from a weak to a strong magnetic field is also the reason for the storage of charged particles in the main spectrometer. By scattering, these can cause background events.

In general, the electrons in the spectrometer move up to the centre against an E-field and constantly lose kinetic energy. Since the movement vectors of the electrons are oriented antiparallel to the E-field due to the B-field, only electrons with a total kinetic energy greater than the counter voltage applied by the E-field can pass through the spectrometer. Thus it is obvious that the MAC-E filter filters on the basis of the total kinetic energy and does not only consider the parallel component.

The pre-spectrometer works with a static counter voltage of 10.0 keV. As a result, the number of electrons arriving at the main spectrometer is reduced by a factor of  $10^6$ . This reduces the probability of ionisation processes in the main spectrometer of residual gas. It must be taken into account that from an experimental point of view a perfect vacuum cannot be created. Therefore there are some residual atoms in the main spectrometer which can be ionised by the decay electrons, however, the pressure is on the order of  $10^{-11}$  mbar.

The counter voltage in the main spectrometer is dynamically controlled and allows the scanning of the electron energy spectrum. This corresponds to an integrative measurement. The filter function of this type of measurement can be described by a transmission function. The following applies

$$\frac{dN(qU_0)}{dt} \propto \int_{qU_0}^{E_0} \frac{d^2N}{dEdt}(E_0, m_{\nu_e}^2) \cdot T(E, qU_0) dE \quad (2.4)$$

the integration limits are determined by the counter voltage  $U_0$  and the endpoint energy  $E_0$ , the integrand consists of the differential tritium spectrum as well as the transmission

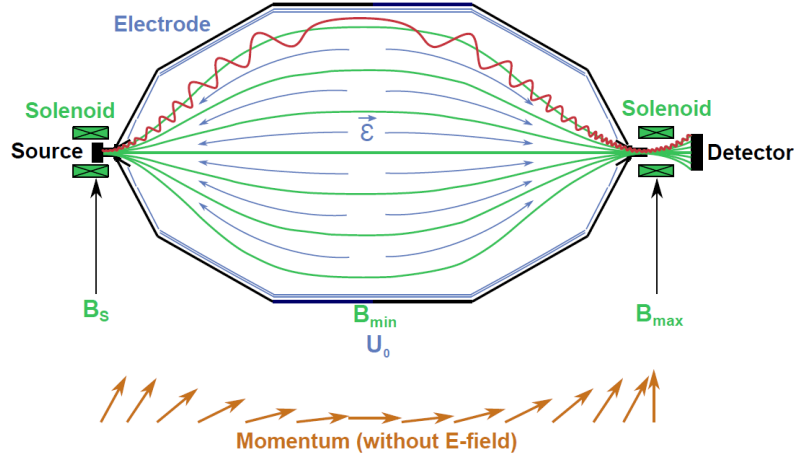


Figure 2.5.: The MAC-E filter principle. Electrons are guided adiabatically along the magnetic field. Up to the analysis level an electric counter field is applied, which filters all electrons with not enough kinetic energy. [6]

function  $T$ , which can take on values between 0 and 1, see equation 2.5. The combination of the transmission function with the energy loss distribution gives a complete response function of the experiment. For further details see [7].

$$T(E, qU_0) = \begin{cases} 0 & E < |qU_0| \\ \frac{1 - \sqrt{1 - \frac{E - qU_0}{E} \cdot \frac{B_s}{B_{\min}}}}{1 - \sqrt{1 - \frac{B_s}{B_{\max}}}} & |qU_0| \leq E \leq |qU_0| + \Delta E \\ 1 & E > |qU_0| + \Delta E \end{cases} \quad (2.5)$$

The accuracy of the scanning is determined by the ratio of the B-field strengths, which determines the perpendicular component of the kinetic electron energy. According to 2.1 the following applies

$$\Delta E = E_{\text{kin,max}} \cdot \frac{B_{\min}}{B_{\max}}. \quad (2.6)$$

In the current default setting [37] the energy resolution is  $\Delta E = 2.77$  eV. Originally, a resolution of  $\Delta E = 0.93$  eV could be achieved [5]. The reason for the difference is the attempt to reduce the background. For this, the magnetic field strength  $B_{\min}$  is increased in order to obtain a smaller flux tube. As described in the chapter 2.3, this measure allows an effective background reduction at the expense of filter accuracy.

### 2.2.4. Detector

At the end of the 70 m long KATRIN experiment there is the detector with a diameter of 9 cm. As shown in figure 2.5, the detector is surrounded by two cylindrical coils which focus the magnetic flux tube to detector size. The detector based on p-i-n semiconductor

technology achieves an energy resolution on the order of 2 keV in an energy interval of 5-50 keV. To reduce backscattering and the intrinsic detector background, the electrons are accelerated by 10 keV via the Post Acceleration Electrode (PAE) shortly before the detector. In total the detector consists of 148 individual pixels, which all have the same area and are divided into 13 rings, see figure 2.6. In addition to the energy measurement, the location of the electron impact on the detector surface is also of interest, since the magnetic field at the detector points directly back to the origin of the electron within the WGTS. This enables the reconstruction of the trajectory and thus the subsequent filtering out of events which originate outside the flux tube. [37]

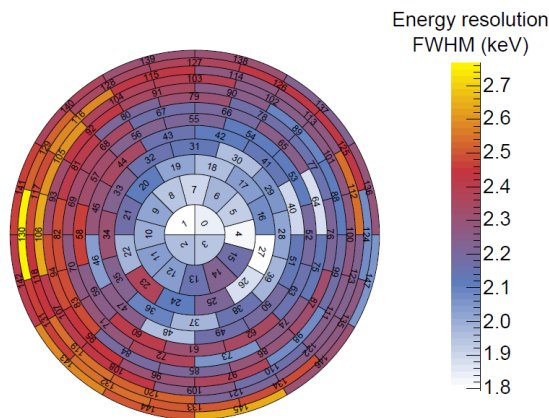


Figure 2.6.: Calibration measurement of the detector to determine the energy resolution. The 148 pixels have different resolutions. If the differences are too big, some pixels will be excluded from the analysis. [6]

## 2.3. Background in the Main Spectrometer

The control over the parameters and boundary conditions of an experiment always determines the accuracy of the experimental statement. With its 70 m length, the KATRIN experiment offers a multitude of parameters and thus possible disturbing factors. Examples are the column density of tritium in the WGTS, the vacuum in the main spectrometer, the counter voltage in the MAC-E filter and many more. Statistical and systematic errors can occur at all these points. The statistical error describes the random fluctuations of a measurand, while the systematic error includes calibration errors and model quantities that are not considered. In this context the background noise, which is important for the thesis, is to be classified. These are unwanted events which superimpose the measurement results, i.e. a diffuse systematic error. A precise model description enables the embedding of the unspecific background in the space of experimentally clearly describable parameters. The source of most of the background is found in the main spectrometer itself. The predecessor experiments Troitsk and Mainz show that this background does not scale directly with the size of the spectrometer. Troitsk is about four times as large as Mainz and both have a background of 10 mcps [4]. This allows the prognosis that a comparable background

rate is possible with KATRIN. Currently the background is about 300 mcps depending on the experimental setup.

The MAC-E filter has an enormous influence on the background. On the one hand, all events with an energy lower than the counter voltage are cut off. On the other hand, the flux tube causes all existing electrons to be directed towards the detector and electrons which are created in the analysis volume itself are accelerated according to the electrical potential on site. This shows that electron sources within the main spectrometer are of particular importance for background observation.

In the following sub-chapters the characteristics of the background are described in more detail. The original primary background of KATRIN comes from radon decays in the main spectrometer. After the installation of copper baffles, this background component has decreased by  $(95.1 \pm 0.3)\%$  [6] in the SDS-II campaign, so that a Poisson distributed background is currently dominant. As Rydberg atoms are considered to be the source of this component, this is referred to as the Rydberg background, see chapter 2.3.2. The last chapter deals with sputtering, the central mechanism in this work for producing Rydberg background from  $^{210}\text{Pb}$ .

### 2.3.1. Radon

Radon is a radioactive noble gas of elementary importance for background observation. Essentially only three isotopes occur in nature, namely  $^{222}\text{Rn}$ ,  $^{220}\text{Rn}$  and  $^{219}\text{Rn}$ , whereby  $^{222}\text{Rn}$  with 90% occurs most frequently and plays a special role in background analysis. Therefore, in the following  $^{222}\text{Rn}$  is dealt with separately from  $^{220}\text{Rn}$  and  $^{219}\text{Rn}$ . In the context of astroparticle-physical experiments it can be stated that radon exposure is a high experimental challenge, for example for GERDA and BOREXINO [40]. Thus the following considerations on radon are also important for the conceptual understanding of other experiments.

#### $^{220}\text{Rn}$ und $^{219}\text{Rn}$

For background observation, electrons generated in the flux tube are of particular importance, as they can reach the detector with the tritium endpoint energy. In this connection  $^{220}\text{Rn}$  and  $^{219}\text{Rn}$  are interesting. Both are electrically neutral and can therefore move freely, which results in an even distribution in the main spectrometer. During decay, an alpha particle and radioactive polonium are produced. Both particles themselves do not represent a background, but can produce background electrons in different ways. The produced electrons are accelerated and deflected by the existing E- and B-fields, depending on where they are produced. If and with which energy the electron reaches the detector depends on the initial energy, direction of movement relative to the B-field and the starting position. The alpha particle can ionise existing residual gas in the main spectrometer or release electrons through interaction with the spectrometer wall. In principle, there are several ways to generate electrons in polonium. If the nucleus is in an excited state, the excitation energy can be transferred to an electron by internal conversion, which then leaves the atom with an energy of the order 100 keV. It is also possible that the alpha particle, by means of coloum interaction, transfers energy to the electrons as they leave the atom. This can emit electrons with energies in order 1 keV. The atomic relaxation that follows

these processes produces electrons in the 10 keV energy range, while the atomic shell reorganisation is in the eV range. [6]

In total, up to 20 primary electrons can be generated by a radon decay. These electrons can generate hundreds of secondary electrons by trapping them in the MAC-E filter. [6] This cascade of background must be prevented as early as possible. The best point of intervention is therefore to catch the radon before it enters the main spectrometer. The most suitable place for this is between the non-evaporable getter (NEG) pumps and the main spectrometer. These special pumps allow to maintain the vacuum with  $10^{-11}$  mbar, but they are also the largest source of radon in the experiment itself [41]. Due to the installation of liquid nitrogen-cooled copper baffles, a considerable part of the radon condenses on the copper surface. Figure 2.7 shows the experimentally measured background reduction as well as the theoretically expected radon reduction.

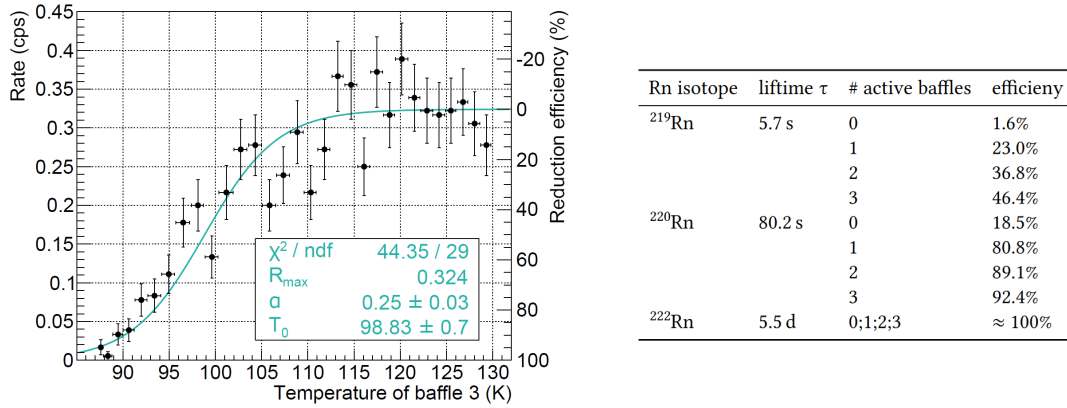


Figure 2.7.: Left: Effect of the copper baffles on the background depending on the temperature. The difference in the background rate between cold and warm copper baffles is about one order of magnitude.[42] Right: Model results for expected radon reduction depending on the active baffles. [43]

The radon background rate has been reduced by 95% [6]. The radon reduction due to the copper baffles is therefore significant. As a consequence it is possible to observe new characteristics of the remaining background. These are summarised in chapter 2.3.2.

### $^{222}\text{Rn}$

The effect of  $^{222}\text{Rn}$  is almost zero according to table 2.7. This is calculated using a simple model according to [44], which only needs to be extended to the main spectrometer [43]. The basic idea is that the radon emitted by the NEG pumps can only follow three different paths. It can be pumped out by the TMP, stick to the copper baffles or decay in the main spectrometer. All three processes have a characteristic half-life. This allows a ODE to be set up to calculate the number of particles, see equation 2.7. By simply solving the

equation 2.8 the probability of a decay in the spectrometer can be calculated.

$$\frac{dN(t)}{dt} = -(\lambda_{\text{adsorption}} + \lambda_{\text{TMP}} + \lambda_{\text{decay}})N(t) \quad (2.7)$$

$$P_{\text{decay}} = \lambda_{\text{decay}} \int_0^{\infty} N(t) dt \quad (2.8)$$

The pump efficiency is the difference of one minus the probability of decay. For the concrete calculation the pumping efficiencies of the baffles and TMPs are required, see [43]. Thus the central difference between  $^{222}\text{Rn}$  in comparison to  $^{220}\text{Rn}$  and  $^{219}\text{Rn}$  is the half-life. At 3.82 days, the half-life of  $^{222}\text{Rn}$  is about four orders of magnitude greater than that of  $^{219}\text{Rn}$  [45]. According to the equation 2.8, this reduces the decay probability in the spectrometer and increases the pump efficiency. The significance of  $^{222}\text{Rn}$  in live operation is negligible.

Nevertheless  $^{222}\text{Rn}$  plays an important role in background analysis. The reason for this is the unintentional contamination by  $^{222}\text{Rn}$  during the construction of the experiment [6]. In this phase the inner electrode has been installed in the main spectrometer. For this purpose a good breathing air supply for the workers must be guaranteed permanently. Through the constant air flow of the external breathing air supply, radon particles enter the interior of the spectrometer, which can cause an average of about 50 radon decays per second and cubic metre [46]. If these radon atoms decay near the spectrometer wall, it is possible that the daughter nucleus is implanted in the spectrometer wall. Via the known uranium-radium decay chain, see figure 2.8, it can be seen that the long-lived  $^{210}\text{Pb}$  accumulates in the spectrometer wall as a result of this process. These near-surface alpha emitters can catapult atoms, ions and electrons into the interior of the main spectrometer in case of decay. These particles are directly or indirectly able to generate background signals. This process leads to the Rydberg background.

### 2.3.2. Motivation of Rydberg model

The background existing in the KATRIN experiment is not due to a single process, but is of multivariate nature. This can easily be shown by means of figure 2.9. Here the background rate of the respective pixel ring is plotted over the corresponding radius in the analysis plane. The background rate is normalised to the observation volume of the respective ring. This allows a rate comparison between different experimental setups. In the figure it can be clearly seen that the background rate increases towards the outer edge of the flux tube. This behaviour can be observed in all background measurements with normal boundary conditions. Thus the background rate contains a spatially inhomogeneous component in the spectrometer. Since  $^{220}\text{Rn}/^{219}\text{Rn}$  produce a spatially homogeneous background, another cause can be found.

By installing the copper baffles, the radon induced background has decreased considerably. This is expressed by a Poission distributed background rate, see figure 2.9. Although the radon decays are Poission distributed like all radioactive decays, their effect on the background is not Poission distributed. This is due to the fact that the decay events trigger a cascade of electrons, which carry a strong temporal distortion. Therefore, radon can be excluded as the main cause of the currently dominant background component. After

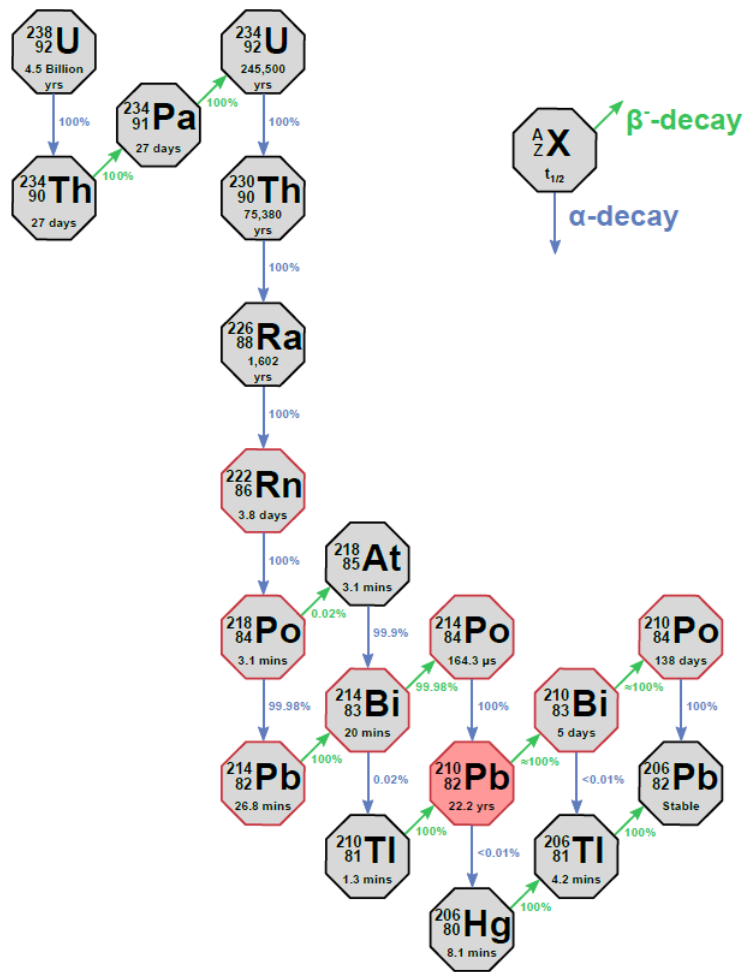


Figure 2.8.: Uranium Radium decay chain. The central decay path of  $^{222}\text{Rn}$  for the KATRIN experiment is outlined in red [6]. Originally modelled [47].

the discovery of this correlation, many background measurements have been carried out in order to learn more about the characteristics of the background. A main focus is on the influence of the B-field, the voltage between spectrometer and inner electrode, the pressure and the effect of an artificial Co60 contamination. A full insight into the most important analyses can be found in [6] and [7].

**Baking** The baking of the spectrometer has a great influence on the background. This has been tried out for the first time between the SDS-IIA and SDS-IIB series of measurements. Here the spectrometer is heated to about  $200\text{ }^\circ\text{C}$  for 8 days. The strong heat primarily evaporates the thin water layer on the spectrometer wall and the copper baffle. Due to the free surface the adsorption capacity of the baffles is regenerated and the partial water pressure is reduced by two orders of magnitude. This is reflected in a pressure change from  $3 \cdot 10^{-10}$  mbar to  $6 \cdot 10^{-11}$  mbar. The total background reduction from SDS-IIA to SDS-IIB amounts to 40%, see figure 2.10. It should be noted at this point that the spatial

## 2. KATRIN Experiment

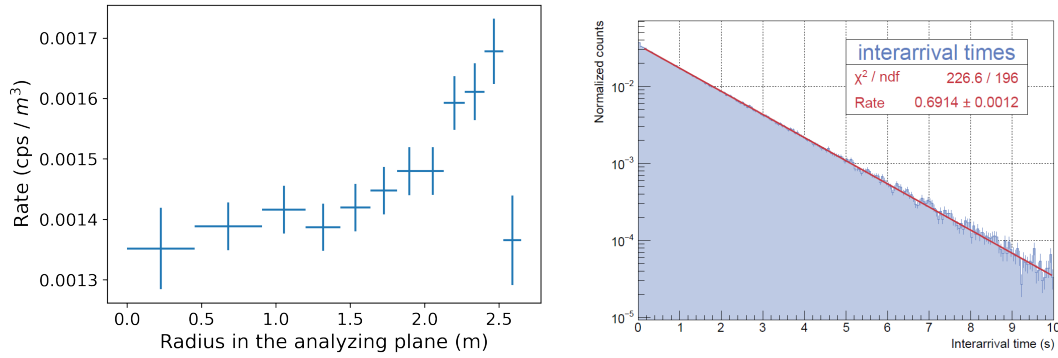


Figure 2.9.: Left: Radial distribution of the background rate during the KNM2 periode 2 measurement phase, run list see A.3. The background grows to larger radii on analysing plane. Rate on last ring is lower because of pixel shadowing. Right: Background in dependence of the inter arrival time. The distribution is compatible with an exponential fit. The background therefore follows a Poisson distribution.[7]

distribution of the background is hardly changed by the baking process.[6]

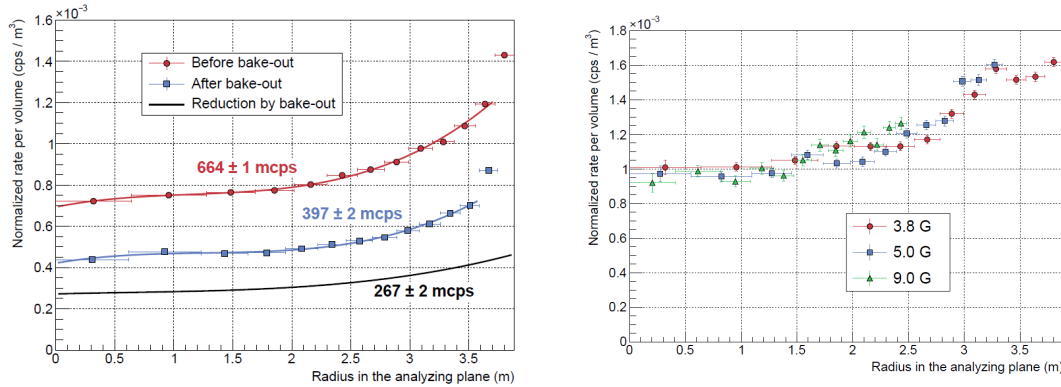


Figure 2.10.: Left: Background reduction by baking the main spectrometer for several days. The reduction is almost constant over the radius of the analysis plane. The last data point is excluded from the analysis because the rate is too low. Probably the ring is shadowed. [6] Right: Background reduction by changing the B-field. Form of the background rate remains the same, therefore reduction is only due to reduced observation volume.[6]

**B-Field** The behaviour of the background rate at different magnetic field strengths is very informative for the further characterisation of the background. In general, variations in the magnetic field strength can change the size of the flux tube volume. The higher the magnetic field  $B_{\min}$ , the smaller the flux tube volume. As expected, at a high magnetic field strength, the total background rate decreases with the reduction of the flux tube volume, but the shape of the background remains the same, see figure 2.10. The

reduced background rate is mainly due to the smaller observation volume. Therefore, the inhomogeneity cannot be explained by low-energy charged particles coming from the spectrometer wall. These would have been more strongly shielded by the magnetic field. The dominant generation mechanism must therefore generate spatially homogeneously distributed background electrons.[6]

**<sup>60</sup>Co Contamination** Photons of the natural radiation background such as from <sup>40</sup>K would be a possible cause for the background. These could release electrons from the metallic surfaces of the spectrometer or directly ionise residual gas. To verify this hypothesis, an artificial <sup>60</sup>Co source with an activity of 53 MBq is placed about one meter away from the main spectrometer. The effects of the radioactive source depend on the operating setting of the B-field. In the asymmetrical case, electrons are guided from the spectrometer wall directly to the detector. Here the <sup>60</sup>Co contamination can clearly be observed. In the symmetrical normal operation no cobalt signal can be noted. This generally excludes all low-energy electrons coming from the wall of the spectrometer as the cause, regardless of how they were generated. The magnetic shielding and the inner electrode efficiently suppress this component. [48]

**Pressure** Another parameter that influences the background is the pressure in the main spectrometer. The higher the pressure, the greater the probability that high-energy electrons will generate further electrons by inelastic collisions with the residual gas. Thus, the importance of synchrotron radiation as a cooling down mechanism compared to ionisation decreases [49]. Since a collision cascade is the source of many secondary electrons, the background should increase at higher pressure, see figure 2.11. A differentiated approach shows that the background increases mainly at the edge of the flux tube. A possible explanation for this is provided by high-energy electrons in the keV range. Thus according to equation 2.9 a conversion electron of <sup>210</sup>Pb has a cyclotron radius of 1.1 m, where B=0.6 mT and  $v_{\perp} = 0.37c$ .

$$r = \frac{mv_{\perp}}{|q|B} \quad (2.9)$$

Secondary electrons would move on the same magnetron radius and could enter the outer flux tube volume by scattering. With a small radius on the analysing plane the background remains almost the same. This is difficult to reconcile with the thesis that low-energy electrons from the spectrometer wall create the background. This is because an increased pressure is accompanied by a shorter storage time and thus a shorter drift length[50]. Therefore, the background in the inner flux tube volume would have to decrease. It should be noted that in addition to <sup>210</sup>Pb, muons or general background radiation can also generate high-energy electrons.

**Inner electrode voltage** It can generally be stated that the background is strongly dependent on the voltage between the spectrometer wall and the inner electrode. This can be seen in figure 2.12. From this it can be deduced that the source of the residual background is in the wall area.

## 2. KATRIN Experiment

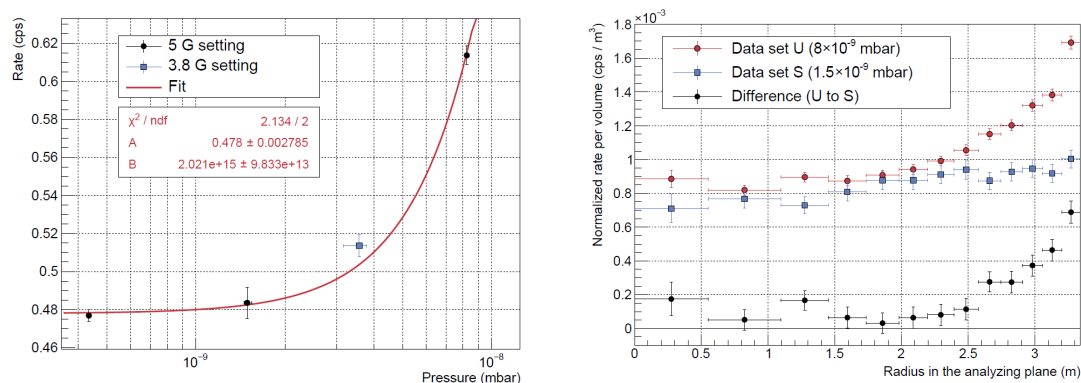


Figure 2.11.: The data were recorded during the SDS-II measurement campaign. Left: Background rate as a function of pressure. The higher the pressure the bigger the background. Right: Comparison of two data sets at different pressures depending on the radius of the analysing plane. The differentiated approach shows that the background increases mainly in the outer flux tube volume. [6]

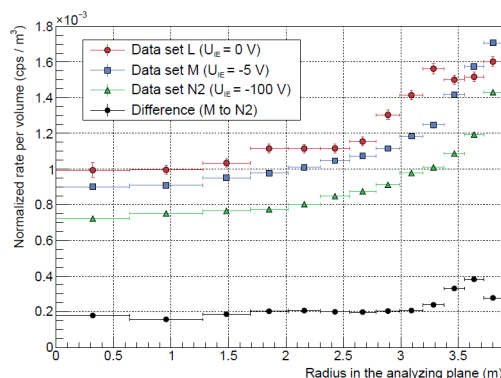


Figure 2.12.: Background depending on the voltage of the inner electrode. The background rate decreases with increasing voltage almost independently of the radius. [6]

In summary, the following statements can be made about the background of the KATRIN experiment. After installation of the copper baffles the background is essentially Poisson distributed. A B-field change in the centre of the spectrometer leads to a smaller background, but the reduction is mainly due to a smaller observation volume and not to the influence of the stronger B-field on charged particles. 75% of the background is homogeneously distributed in the flux tube volume, while 25% of the events take place at the outer flux tube, see figure 2.9 [6]. The influence of the inner electrode in addition to the above mentioned, indicates an electrically neutral source of low-energy electrons, which has its origin near the spectrometer wall. Rydberg atoms can fulfil the described characteristics.

In the following chapter the Rydberg background model will be outlined in more detail.

### 2.3.3. Rydberg model

Rydberg states are defined as highly excited atomic states with quantum numbers in the order of  $n > 10$  [51]. These are possible in most atoms and in many diatomic molecules and ions [51]. Due to the high excitation of one of the shell electrons, the location expectation value is located far away from the nucleus and the other shell electrons. Therefore, the system can be regarded as a hydrogen atom with a heavy nucleus in good approximation. In particular the well-known energy formula of the hydrogen atom, see equation 2.10, is used in the description of the Rydberg atom [7].

$$E_n = \frac{R_y}{n^2} \quad (2.10)$$

Here  $R_y$  stands for the Rydberg constant with 13.6 eV and  $n$  corresponds to the excitation level. From formula 2.10 it can be seen that the energy distance between two states decreases rapidly with the quantum number  $n$ . Already with the quantum numbers from  $n = 7$  to  $n = 8$  the energy difference is smaller than 0.07 eV. This is of special interest because in the context of KATRIN the interaction of the Black Body Radiation (BBR) with the Rydberg atoms is relevant. As can be seen in figure 2.13, the most probable BBR energy is 0.07 eV. Thus, from an energy point of view, an interaction with Rydberg states is possible.

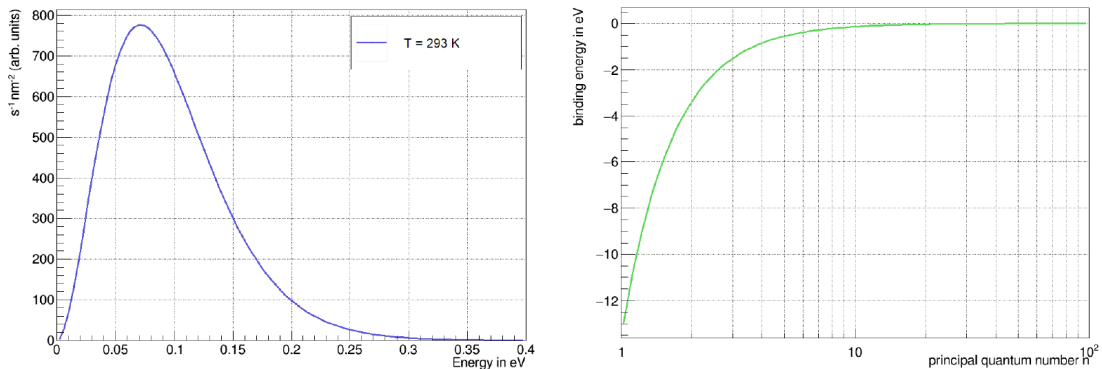


Figure 2.13.: Left: BBR spectrum at T=293 K. According to Planks law a peak at 0.07 eV can be observed. Right: Hydrogen Energy stats as a function of  $n$ . The ionisation energy converges quick to zero. [8]

According to Harms [6] there are three relevant process options for Rydberg atoms. These are spontaneous decay, stimulated transmission and field ionisation.

In spontaneous decay the Rydberg atom returns to its ground state by emitting a gamma quantum. The lifetime  $\tau$  is proportional to  $n^3$  and  $l(l+1)$  [52]. For high excitation states, this allows a decay lifetime in the millisecond range [7]. Such a long lifetime is a basic requirement to be the cause for the homogeneously distributed background in the context of the KATRIN experiment [7].

There are three different variations of the stimulated transmission provided by the BBR. Excitation, de-excitation or ionisation of the Rydberg atom can occur. The possibility of ionisation deserves special attention at this point, as this could be a central production

mechanism to motivate the generation of low-energy electrons in the sensitive flux tube volume. The probability of ionisation is determined by the cross section  $\sigma$  and the photon density  $n_\gamma$

$$P_{\text{nl}}^{\text{ion}} = c \int_{1/2n^2}^{\infty} d\omega \sigma_{\text{nl}}^{\text{ion}}(\omega) n_\gamma(\omega). \quad (2.11)$$

The difficulty lies in determining the cross section. A practicable analytical representation of the matrix element of the interaction can be found [53]. From this formula Trost [7] calculates that the emitted electrons have energies  $<0.12$  eV and that the probability of ionisation according to simulation results is  $1.128\%$ . Thus Rydberg atoms seem to be not only a qualitatively but also a quantitatively explanation for the observed background. The last important interaction with Rydberg atoms is the field ionisation. The basic principle is shown in figure 2.14. An external E-field causes a displacement of the potential well and the electron in the excited state is ionised earlier.

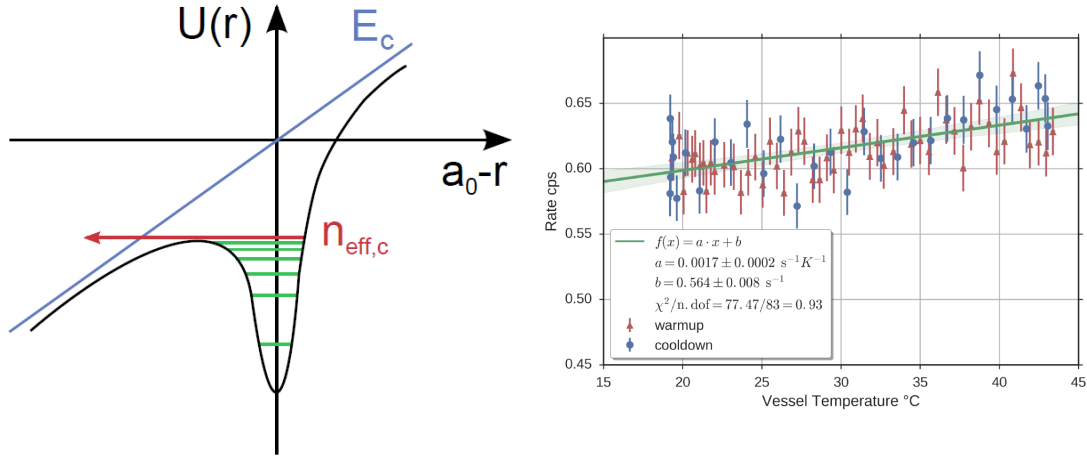


Figure 2.14.: On the left: Principle of Field Ionisation. An external E-field causes a displacement of the potential well. This results in a correction of the quantum number  $n$ , which allows earlier ionisation.[6] inspired by [54]. Right: Background as a function of temperature. A linear increase with the vessel temperature can be observed. [7]

In the inner part of the main spectrometer the E-fields are too weak to be relevant for field ionisation. However, strong E-fields are present at the beginning and end of the main spectrometer and between the spectrometer wall and the inner electrode. The early ionisation of Rydberg atoms between spectrometer wall and inner electrode would therefore be a process dependent on the internal electrode voltage. This could fit to the results of figure 2.12. This explanatory model strongly suggests a Rydberg based background model. [7]

Furthermore a temperature dependence of the background can be observed, see figure 2.14. This agrees with the expectation that BBR intensity increases with increasing temperature. According to the simulation results of Trost [7], an increased ionisation rate of  $7.3\% \pm 2.1\%$

can be expected with a temperature increase from 19°C to 43°C. The measured increase of  $6.8\% \pm 0.7\%$  is in agreement with this.

There are several ways to motivate the presence of Rydberg atoms in the main spectrometer [6]. In this thesis the focus is on sputtering as a generation mechanism. As we have seen, the Rydberg model can explain the remaining background characteristics. However, a high level of excitation of the Rydberg atoms is necessary, as this requires a longer lifetime [7]. Only a lifetime in the *ms* range can explain a homogeneous distributed background. The basic problem is that with sputtering the probability of a high excitation state decreases with  $n^{-3}$  [7]. A possible solution to this problem is offered by sputtered ions, which can account for about 5% of the sputtered particles. Ions have the advantage of higher energy due to the voltage potential in the spectrometer and can move faster. Furthermore, sputtered particles have a higher energy for purely kinematic reasons, as they are produced by inelastic interaction [55]. This enables a homogeneous distribution even with shorter lifetimes. Therefore, the focus in the following analysis is on sputtered ions. Another key element of this investigation is the electron capture of a sputtered particle. This enables the necessary electrically neutral state of the Rydberg atom. This leads to the use of Geant4 as stimulation software, as will become clear in the following chapter 2.4.

## 2.4. Sputtering

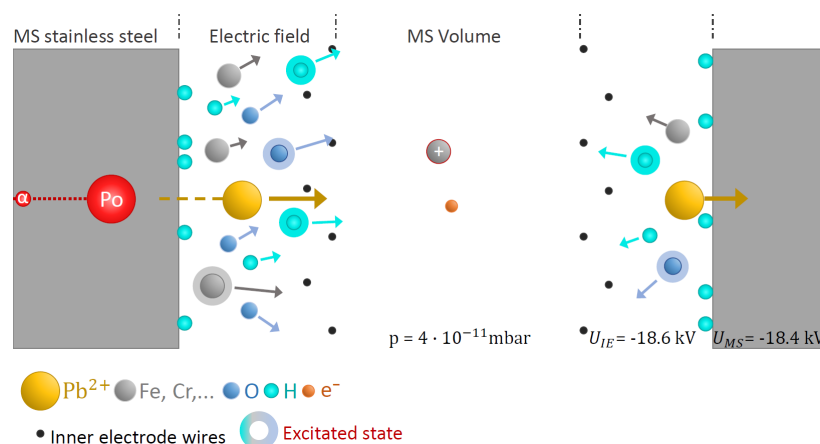


Figure 2.15.: Sputtering in the context of KATRIN. In the spectrometer wall a  $^{210}\text{Po}$  nucleus decays into  $^{206}\text{Pb}$ . The recoil energy enables the double positively charged lead core to release some particles from the spectrometer wall. The sputtered particles are then located in the spectrometer volume and are influenced by the E-field of the inner electrode. [56]

As can be seen from chapter 2.3.1, sputtering is caused by the radioactive decay of  $^{210}\text{Pb}$  respectively  $^{210}\text{Po}$ . It can be seen as a possible root of the residual background in the spectrometer. In the following subchapter sputtering in general will be described in more detail. The aim is to enable a qualitative classification of the topic.

Sputtering describes the effect of a projectile when it hits the target, the solid. The projectile

can be atoms, ions or molecules, which hit the solid with kinetic energies from eV to MeV. The target can be of any complexity, from a simple crystal structure to an amorphous solid. In most cases, however, only near-surface layers are of interest for sputtering. Depending on the energy and the materials used, a penetration depth in the nm to  $\mu\text{m}$  range can be expected. The main effect of sputtering is the removal of atoms from the solid structure and a possible implantation of the projectile particles in the solid. The particle or projectile source is usually outside the target, in the KATRIN application the source is found in the form of  $^{210}\text{Pb}$  inside the target, see figure 2.15. Thus, sputtering is used in surface analysis and surface treatment. [57]

An important parameter of the process is the sputtering yield. It is known as

$$Y = \frac{\text{Number of atoms removed}}{\text{Number of incident particles}}. \quad (2.12)$$

The sputtering yield depends strongly on the experimental design and often ranges from  $10^{-5}$  to  $10^3$  [58]. The ion fraction is usually <5% [57].

To remove an atom, the kinetic energy perpendicular to the surface must be greater than the binding energy. In rough approximation, the binding energy can be equated with the sublimation energy [59], which is  $\mathcal{O}(\text{eV})$  [57].

If the projectile energy is in the keV range or smaller, atomic collisions and the resulting collision cascades dominate, which distribute the energy in the solid. If the projectile consists of ions, from MeV onwards the energy transfer to electrons must also be taken into account. These couple to phonons and thus lead to strong local heating, which leads to the vaporisation of further atoms. This phenomenon can be observed especially in semiconductors and insulators. Therefore, evaporation is not to be expected in the metallic spectrometer wall of KATRIN. [57]

A well applicable theory for the detailed processes in sputtering was published in 1969 by Sigmund [60]. The core statement of the theory is the prediction of the sputter yield as a central parameter as well as the energy and angle distribution.

According to Sigmund [60], the average number of atoms with a certain energy  $E_i$  in a linear cascade follows the following distribution

$$F(E_n, E_i) = \Gamma \frac{E_n}{E_i^2} \quad (2.13)$$

$E_n$  describes in this context the primary projectile energy. Thus F can be interpreted as a kind of recoil density. It should be noted that the internal energy density decreases quadratically. With the help of this equation, material-specific dependencies can be integrated into the model. Finally, the sputter yield results from a linear relationship to the energy output near the surface.

$$Y = \Lambda F_D(E_0, \Theta_0, x = 0) \quad (2.14)$$

Here  $\Lambda$  contains specific material properties and  $F_D$  reflects the energy transfer in the surface area. It is generally assumed that  $F_D$  is proportional to the nuclear stopping

crosssection. Sigmund derives the following differential sputter yield equation from these expressions in [60]

$$\frac{dY^3}{dE d\Omega^2} = F_D(E_0, \Theta_0, x = 0) \frac{\Gamma_m}{4\pi} \frac{1 - m}{NC_m} \frac{E}{(E + U)^{3-2m}} \cos(\Theta). \quad (2.15)$$

The parameter  $m$  is related to the interaction potential via  $V(r) \propto r^{-1/m}$ ,  $C_m$  and  $\Gamma_m$  depend on the cross section and  $N$  stands for the target density. Equation 2.15 brings the central findings of sputtering research to a point. According to formula 2.15 the sputter yield follows a cosine distribution depending on the  $\Theta$  angle. This behaviour is rarely observed experimentally [57]. In general the angle dependence depends on energy, mass and the target surface structure. This results in an additional fit parameter  $y$  in the form of  $\sim \cos(\Theta)^y$  [57]. However, even this correction is not generally valid. Especially for ions, a peak can be observed in the mirrored direction to the perpendicular of the direction of incidence [57]. This leads to a peak at about  $45^\circ$  in the case of an isotropic particle flow towards the surface, whereby a strong variance is also present here. Since the  $^{210}\text{Po}$  recoil core is doubly negatively charged, there is no cosine distribution according to the formula 2.15 is to be expected.

However, a fundamental and therefore numerical approach is more suitable for calculating the effect of sputtering on the background of the KATRIN experiment. The basis of the analysis is a Monte Carlo simulation, which calculates the physical interaction of projectile particles with shielded potentials. This allows the determination of momentum transfers on an atomic basis and avoids analytical approximations. Each interaction is calculated individually during the simulation. Geant4 [61] is the simulation framework used for this. In contrast to the SRIM [62] programme, which is also widely used, Geant4 allows the integration of complex geometries and the calculation of ions. With regard to the Rydberg background, the consideration of ions is of particular importance, as shown in chapter 2.3.3. In the KATRIN context, SRIM has been used as standard for sputtering simulations like in [8] and [7]. The change to Geant4 should enable a more in-depth simulation.

Details about the mechanics behind the Geant4 Simulation can be found in chapter 3.2.



## 3. Methods of Geant4-based simulations

Geant4 [63] is a simulation toolkit written in C++ for simulating the interactions of particles with matter. It is based on Monte Carlo methods and has been developed by the high-energy physics community at Cern. Due to continuous development of the simulation program, the fields of application range from high-energy particle physics to medical physics, materials science and space ship design. This broad range of applications makes Geant4 a very useful tool for a variety of experiments, such as Borexino [64], CREST-II [65] and Cern [66].

In the following, Geant4, which is the software on which the simulation is based, will be explained in more detail. The aim is to give a rough overview of the general software structure and the specifically implementation. Chapter 3.1 explains central terms for working with the Geant4 software and introduces the classes that are essential for every Geant4 programme. Finally, chapter 3.2 outlines the simulation on which the work is based.

### 3.1. General programme flow and Mandatory classes

Basic terms in Geant4 context are event, track, step, trajectory, process and run. These terms are explained briefly below.

An event is a stack of primary particles. A track is a snapshot of one particle and includes variables such as location, energy, track ID and particle name. Step is the delta information between two tracks. The Trajectory contains the complete history of a track. The process is particularly fundamental, as it implements physical or navigational interactions. A run is a series of events. These terms can be used to describe essential functions of Geant4.

The basic structure of Geant4 is the same for every application. At the beginning there is the initialization of geometries, materials, particles, physical processes and other parameters. The command *BeamOn* indicates the begin of a Run. During a run the geometry is fixed and a loop over all events takes place. Finally, after the completion of a run, any number of further runs can be started. The run manager is the central administration instance and ensures a smooth program run.

Geant4 gives the user a great deal of programming freedom and only defines very rough guidelines for the program structure. In principle, only three classes need to be implemented by the user. These are a construction, physics and particle generator class. These must inherit from the Geant4 provided base classes *G4VUserDetectorConstruction*, *G4VUserPhysicsList* and *G4VUserPrimaryGeneratorAction*. In most cases it is useful to create additional user classes, a selection of optional classes is shown in table 3.1.

The mandatory classes are described in more detail below.

Table 3.1.: Mandatory and optional user classes with short description. For a complete description see [61].

	Classes	Description
mandatory	G4UserDetectorConstruction	Define of the geometries
	G4UserPhysicsList	Activating relevant physics
	G4UserPrimaryGeneratorA.	Primary particle generation
optional	G4UserRunAction	Provides useful methods during a run like booking Histograms
	G4UserEventAction	Contains all Inputs and Outputs of Event
	G4UserStackingAction	Manage processing Priority of G4Track
	G4UserTrackingAction	User access to Tracking information
	G4UserSteppingAction	User access to Stepping information

### G4UserDetectorConstruction

The geometry of the specific problem is defined by its own design class. Each construction class starts with the definition of a world volume. All other volumes, also called daughter volumes, must be located within this volume. By assigning shape, physical properties and position, the daughter volumes achieve a concrete physical manifestation. The assignment of properties works via the classes G4VSolid, G4LogicalVolume and G4VPhysicalVolume. An exemplary implementation is shown in figure 3.1.

```

G4Box*
sWorld = new G4Box("World",           //name
                fWorldSizeX/2,fWorldSizeYZ/2,fWorldSizeYZ/2); //dimensions

fLWorld = new G4LogicalVolume(sWorld, //shape
                              fWorldMaterial, //material
                              "World"); //name

G4VPhysicalVolume*
pWorld = new G4PVPlacement(0, //no rotation
                          G4ThreeVector(0.,0.,0.), //at (0,0,0)
                          fLWorld, //logical volume
                          "World", //name
                          0, //mother volume
                          false, //no boolean operation
                          0); //copy number

```

Figure 3.1.: Commented sample code for the implementation of a World Volume.

### G4UserPhysicsList

The physics list created by the user fulfills the purpose to consider only those parts of physics relevant to the problem. If, for example, the Compton effect with photons is to be considered in a simulation, but not the photoelectric effect, a separate process activation is possible. In addition, cuts for particle production can be introduced. If required, only the interactions of primary particles and not of secondary particles can be simulated.

The cutoff corresponds to the minimum required mean free path length. If a secondary particle can no longer propagate this far, it is not generated in the first place. Internally, Geant4 converts the length into an energy depending on the material and particle type. By using a cutoff length instead of an energy, a spatially precise particle stop is possible. The use of cutoffs is associated with a considerable reduction in the overall calculation effort. Furthermore, all particles important for the simulation are defined in the physics list. Since many problems require similar physics lists, there are a number of predefined lists, see [67]. In the context of the master thesis none of these predefined lists can be used. However, with a few changes it is possible to use the modular physics list used in the Geant4 electromagnetic exercise programme.

#### **G4VUserPrimaryGeneratorAction**

The generation of primary particles is made possible by the `G4VUserPrimaryGeneratorAction` class. Particle Gun and General Particle Source are available. The General Particle Source enables a more differentiated source description than the Particle Gun. However, this is not used in this thesis. By calling up the Particle Gun, the particle type, initial energy, location, impulse, direction of motion and polarisation are determined.

## **3.2. Simulation setup**

Depending on the application there are a large number of Geant4 own classes from which the user can derive his own variation. Inheriting in the object-oriented C++ language is essential for this. If the methods of a Geant4 class are helpful, a user-specific class adapted to the problem can be created by inheritance.

In this context the five optional User Action classes are of particular importance. These virtual classes are designed to give the user as much control as possible over the simulation. Therefore, these classes are the ideal entry point for user-specific simulation settings in addition to the necessary classes.

Macro is a fundamentally important programme complement. It allows dynamic changes of the simulation after compilation of the programme. For example in the `PrimaryGeneratorAction` class the primary particle can be a proton, but in the macro it can be changed to  $^{210}\text{Pb}$ . In general a macro is a simple .txt file, which is passed to the executable program as a parameter. Thus macro changes are fast and easy to make.

The Geant4 simulation on which the work is based consists of 19 source files with the corresponding header files. A part of the code is taken from the extended electromagnetic example `Testem7`. In the following the classes `DetectorConstruction`, `PhysListEmStandardNR` and `TrackingAction` are described in more detail.

#### **DetectorConstruction**

As explained in chapter 3.1, the definition of the geometries used and the specification of the materials is the main focus of this class. KATRIN is made of stainless steel type 1.4429 (316LN) [37]. Effectively the stainless steel of the Geant4 materials is a good approximation of it. Therefore `G4_STAINLESS-STEEL` is used for the entire analysis. The exact Geant4 steel composition can be found in A.1 .

For the purpose of analysis, an replica of the KATRIN main spectrometer is not necessary. A simple cuboid would be sufficient. However, the surface roughness of the electropolished metal should be included in the simulation which is a major advantage in comparison to SRIM. For this purpose, it is advisable to use the G4Polyhedra class following the example of CREST-II [65]. By configuring the polyhedra with costumed function a periodic surface roughness can be modelled, see figure 3.2. The valley to mountain distance is approximately 100 nm and is thus in the order of magnitude of electropolished metal surfaces [68].

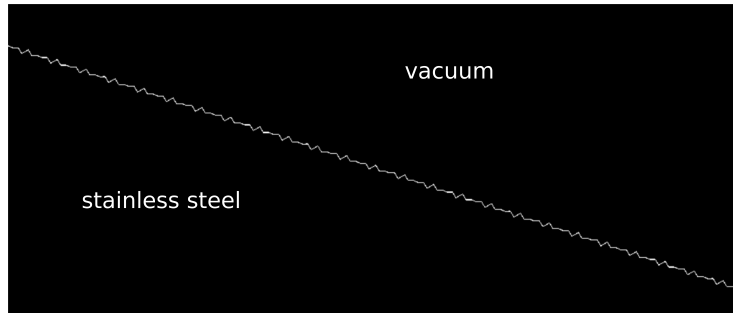


Figure 3.2.: Screenshot of the surface profile from Geant4 Simulation. The periodic mountain valley structure is repeated every 600 nm.

Additionally, a sensitive detector, E-fields and B-fields can be defined at this point. However, this is not necessary for the present investigation.

#### **TrackingAction**

Geant4 offers various options for selecting and saving simulation data. In this implementation all relevant data is collected in the TrackingAction class. The storage is based on the NTuples format, while the selection is achieved by combining different if-conditions. An NTuple consists of an arbitrary large but fixed number of columns. During the simulation these are filled evenly, so that the columns are always of the same length. The data is stored in a .root format and can easily be processed using the uproot package of Python. Of course the use of the root program is also possible.

The central selection condition is the physics process called at the end of a track. For example, when determining the sputtering particles, the last tracking process can only be a transport process, since the particle moves freely in a vacuum.

To determine the implantation depth, it is exactly the other way around. The last tracking process must not be a transport process. In addition, the track ID must be a one, since only the implantation depths of primary particles are relevant.

#### **PhysicsList**

The used physics list is taken from the exercise programme extended electromagnetic example Testem7 from Geant4. This physics list enables the simulation of interatomic scattering based on shielded coulomb potentials. The motivation for the development of this list including the algorithm is to improve the usability of Geant4 [69] in the field of low energy electromagnetic interactions. Therefore it is now possible to use the broad

Geant4 toolkit for sputtering problems or similar. There are no longer any restrictions, for example, with regard to usable geometries as in the SRIM [62] programme, which was used in previous works [8, 7].

The core of the screened Coulomb interatomic scattering in Geant4 is the G4ScreenedNuclear-Recoil class. Its development is based on the widely used SRIM programme. As in SRIM, the universal ZBL<sup>1</sup> screening function is also used [69]. However, the user can also use other screening functions or implement his own. This means that Geant4 has a wider range of functions than SRIM.

The complete physics is based on classical coulomb scattering taking into account the electrical shielding of the nuclear charge. The equation 3.1 corresponds to the basic Coloumb potential including the shielding

$$V(r) = \frac{Z_1 Z_2 e^2}{4\pi\epsilon_0 r} \cdot \phi\left(\frac{r}{a}\right). \quad (3.1)$$

Here the interaction potential  $V$  is calculated from the nuclear charge numbers  $Z_1, Z_2$  and the distance  $r$  of both scattering partners as well as the shielding function  $\phi$  which depends on  $r$  and the parameter  $a$  of the shielding length. The classical problem is shown in figure 3.3 for illustration. With the help of the energy and momentum conservation the classical scattering integral (3.2) can be derived. The following applies

$$\Theta(r) = \pi - 2 \int_{r_{min}}^{\infty} \frac{b dr}{r^2 \sqrt{1 - \frac{V(r)}{E} - \left(\frac{b}{r}\right)^2}}. \quad (3.2)$$

Because of the open upper interval and the singularity at  $r=0$  it is a improper integral. The usual mathematical procedure in such a situation is to substitute the integration variables. In the context of the scattering integral there are various approaches, whereby the Geant4 algorithm uses the equation 3.3 as a substitution [69]

$$x = \frac{x_0}{\cos(\pi z/2)}. \quad (3.3)$$

Furthermore it corresponds to the convention to use dimensionless sizes, it results with  $r = ax$ ,  $b = a\beta$  and  $\epsilon = \frac{E_c}{Z_1 Z_2 e^2 / a}$

$$\Theta(r) = \pi \left(1 - \frac{\beta \alpha(\epsilon, \beta)}{x_0}\right) \quad (3.4)$$

$$\alpha(\epsilon, \beta) = \int_0^1 \sin(\pi z/2) f\left(\frac{x_0}{\cos(\pi z/2)}\right) dz \quad (3.5)$$

$$f(x) = \left(1 - \frac{V(x)}{E} - \frac{\beta^2}{x^2}\right)^{-1/2} \quad (3.6)$$

In connection with the definition of the differential cross section (3.7) the classical problem is completely described

$$\frac{d\sigma}{d\Omega} = \frac{\beta}{\sin(\Theta(r))} \left| \frac{d\Theta(r)}{d\beta} \right|^{-1}. \quad (3.7)$$

<sup>1</sup>Ziegler-Biersack-Littmark

From this point on, the calculation of the cross section and the scattering angle is only possible with numerical methods. The main difficulty is the compatibility of speed, accuracy and stability. Further details of the methods used can be found in [69] and [70].

The calculation of the effective cross section enables the determination of the mean free path length, which indicates the distance between two scatterings. For the calculation of the path length, a minimum transfer energy is used, which must be transmitted at least by an accumulation of impacts. From a physical point of view this procedure is not correct, because the propagation of ions through matter is a continuous scattering process. To make this a discrete process by constructing the mean free path length is justified by the fact that with a small transfer energy the error is negligible. The great advantage of this procedure is the enormous computational acceleration [69].

For the sputtering simulation an extension of the physics list from the predefined exercise program is necessary. The physics of radioactive decays including atomic deexcitation must be added manually to the physics list. Decay physics is essential as  $^{222}\text{Rn}$  and the decay products are responsible for sputtering. It has to be considered that the remaining daughter nuclei are often in an excited state as described in chapter 2.3.1.

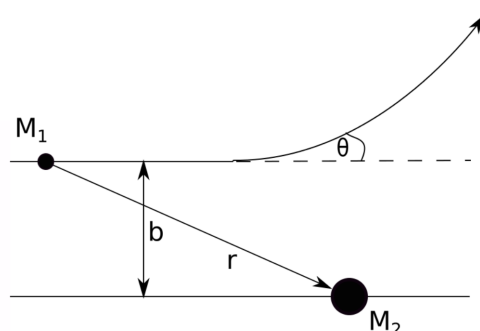


Figure 3.3.: Classical Scattering Problem: Mass one would move on a straight forward path (dotted line), but repulsive potential of mass two results in bended trajectory.

## 4. Sputtering simulation via Geant4

This chapter leads on the basis of chapter 3 through the Geant4 simulation on which the work is based. The aim of the simulation is to estimate the current impact of the early  $^{222}\text{Rn}$  contamination. The focus is on Rydberg atoms, which can enter the inside of the main spectrometer at the end of the decay chain. The workflow of the simulation is based on the real contamination. Thus the programme starts with the implantation of the  $^{222}\text{Rn}$  progenies into the spectrometer wall, see chapter 4.1. The effects of the radioactive decays along the decay chain are shown in 4.2, whereas the sputtering analysis is separately included in 4.3. Finally, the extent of ion sputtering with respect to the background is discussed in chapter 4.4.

### 4.1. Implantation

The implantation of  $^{222}\text{Rn}$  progenies can take place in different ways. In the following, a distinction is made between primary implantation paths and the naive path. The aim of the following argumentation is to find physically motivated starting conditions for the simulation.

The naive way does not know any differentiated transport mechanisms towards the spectrometer wall. This means that no diffusion or electrostatic attraction effects are considered. The basis are the radioactive  $\alpha$  decays of the radon chain with the recoil nuclei. The idea is that a daughter nucleus can move a few  $\mu\text{m}$  through the air due to the recoil energy and then penetrate the surface of the spectrometer wall. Thus,  $\alpha$  decays close to the surface form the basis of the implantation process.

The  $^{210}\text{Pb}$  activity explained by this transport path is estimated in the following by a Geant4 simulation. For simplification only the decay from  $^{222}\text{Rn}$  to  $^{218}\text{Po}$  is simulated. The same implantation rate is taken into account for further  $\alpha$  decays of the Radon chain, but this is only a rough approximation. The recoil energy of  $^{218}\text{Po}$  is 100.7 keV, as shown in figure 4.1, this energy is sufficient to propagate about 100  $\mu\text{m}$  far through air<sup>1</sup>. Therefore a 100  $\mu\text{m}$  deep and 500 nm wide area is defined as the origin of radon decay. The width is motivated by the periodic surface structure. Radon decay is evenly distributed over this effective source area. In the implantation profile, see figure 4.1 it can be seen that a large part of the particles stop near the surface. This is due to the fact that a substantial part of the kinetic energy is released by elastic collisions as a result of the propagation path through the air.

The implantation rate of the radon daughter nucleus  $^{218}\text{Po}$  into the spectrometer wall from the effective original area according to one million processed particles is 23.4%. Along the

---

<sup>1</sup>Air is defined in the simulation by 20%  $\text{O}_2$  and 80%  $\text{N}_2$  at normal atmospheric conditions

decay chain there is a reduction of the implanted atoms, because they can be catapulted out of the spectrometer wall by the recoil energy. This leads to a corrected implantation rate of 11.7% for  $^{218}\text{Po}$ . Besides  $^{222}\text{Rn}$  the  $\alpha$  emitters  $^{218}\text{Po}$  and  $^{214}\text{Po}$  must also be taken into account. For these the same implantation rate is assumed as for  $^{222}\text{Rn}$ . This leads to an effective  $^{210}\text{Pb}$  Implantation rate of 50.6% per  $^{222}\text{Rn}$  decay which has occurred in the effective source area. For the calculation of the expected activity of  $^{210}\text{Pb}$  the following assumptions form the basis. The contamination time is 5 years [6]. The surface of the main spectrometer and the inner electrode are  $1222\text{ m}^2$  [37]. Finally, an average radon activity of  $50\text{ Bq/m}^3$  is assumed [46]. Based on the effective source area, this results in an active volume<sup>2</sup> of  $0.122\text{ m}^3$ . Within the contamination time, an absolute implantation of  $487 \cdot 10^6$   $^{210}\text{Pb}$  atoms is expected. This corresponds to a total activity of 0.68 Bq in the first year after contamination according to the universal law of radioactive decay.

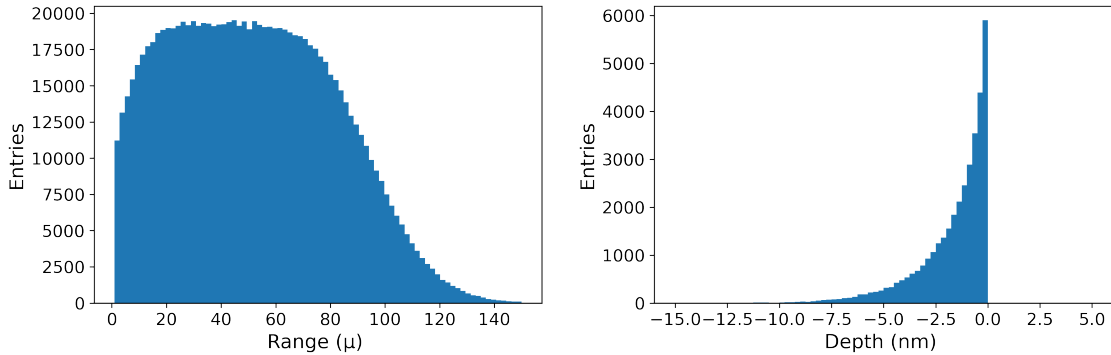


Figure 4.1.: Simulation results with air Left: General range of  $^{218}\text{Po}$  recoil core in air along one axis. One million particle are simulated. Mean range is  $53.4\text{ }\mu\text{m}$  Right: Implantation depth of  $^{218}\text{Po}$  in spectrometer wall. Smooth surface condition.

The naive path can therefore only explain 0.07% of  $^{210}\text{Pb}$  activity based on the 1 kBq estimated activity from Harms [6]. Thus the primary implantation pathways must dominate. This result agrees with the arguments of [6] and [40]. According to Harms [6] there are three primary pathways for KATRIN, each with different mechanisms.

On the one hand, there is direct transport by diffusion. Decisive for the strength of this component is the particle flow onto the surface of the spectrometer wall. In general, the particle flow depends on the concentration  $C$  and the velocity  $v$  of the implantation particles. Over the duration  $\tau$  of the contamination, the concentration can be regarded as constant. This results in a surface concentration  $\sigma$  of

$$\sigma = \sum_{n=1}^4 C_i v \tau. \quad (4.1)$$

In addition to direct transport, there is also indirect transport using aerosols. Here, a further diffusion path towards the surface is created by a combination of radon and its decay products with an aerosol. This works similar to the direct transport but with a speed

<sup>2</sup>active volume =  $1222\text{ m}^2 \cdot 100\text{ }\mu$

that is 10 times slower. In general, the probability of a connection of aerosol with particles is antiproportional to the radius of the aerosol. However, since clean room conditions were realised during the construction of the experiment by means of HEPA filters, this transport path is strongly suppressed.

The last primary transport path is mediated by electric charges. The daughter nuclei of the radon decay chain are all ions and are charged for an average of 20 minutes until they neutralise themselves by impact with the air. During this period of time, charges on the spectrometer wall can attract them and set off a strong transport mechanism.

As can be seen from the qualitative description of the primary implantation pathways, the system to be described is too complex for a simulation to be able to apply it meaningfully. Models with many free parameters would be necessary. For example, there are no real data on the quality of the cleanroom conditions or the accumulation of surface charges. This leaves the indirect way open. A central component of the primary paths is that they start at the surface of the spectrometer wall. Due to the accumulation of radon and its decay products on the surface, the recoil nuclei do not lose energy to the air. This is diametrically different from the naive path. Therefore it makes sense to use vacuum instead of air in the naive way. By this change the implantation mechanism is realistically reproduced. This is characterised by a greater implantation depth, see figure 4.2. However, this simplified approach does not allow any statement about the implantation quantity, because the concrete accumulation on the surface is not simulated. However, there is no absolute necessity for this, since the activity of  $^{210}\text{Pb}$  and thus the implantation quantity is estimable by real measurements [6]. Therefore the original implantation quantity can be calculated retrospectively.

In conclusion, it can be stated that the naive approach using vacuum instead of air provides realistic initial conditions for the simulation. As a simplification of the simulation only the  $^{222}\text{Rn}$  decay is considered as the cause of implantation. The central results of the implantation simulation are the implantation depth. These form the basis for the simulation of the complete decay chain. The results are shown in figure 4.2. The mean depth for a smooth surface is 8.99 nm and thus corresponds to the SRIM results of [8]. The wide interval of the implantation depth for the rough surface is due to the mountain valley difference of about 100 nm.

## 4.2. Decay Chain

$^{222}\text{Rn}$  is part of the uranium-radium series and decays over several  $\alpha$  and  $\beta$  decays to  $^{210}\text{Pb}$ , see figure 2.8. As can be seen from chapter 4.1, the simulated implantation mechanism is based on the recoil energy of the radon daughter nuclei. According to elementary decay kinematics, only the  $\alpha$  decays lead to high recoil energies in the keV range. Thus for the calculation of the implantation distribution of  $^{210}\text{Pb}$  the decay of  $^{222}\text{Rn}$ ,  $^{218}\text{Po}$  and  $^{214}\text{Po}$  is decisive, while the final sputtering is decisively caused by  $^{210}\text{Po}$ . With regard to the implantation distribution the  $\beta$  decays of  $^{214}\text{Pb}$ ,  $^{214}\text{Bi}$ ,  $^{210}\text{Bi}$  and  $^{210}\text{Pb}$  are negligible, but the  $\beta$  electrons can easily leave the spectrometer wall. This fact is considered in the sputter analysis from chapter 4.3.

The change in the implantation depth due to the decays up to  $^{210}\text{Pb}$  are shown in the

#### 4. Sputtering simulation via Geant4

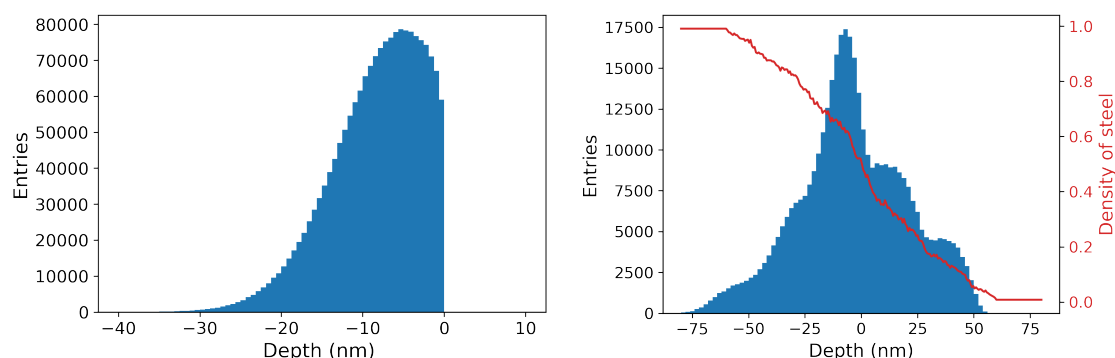


Figure 4.2.: Implantation depth of  $^{218}\text{Po}$ . Left: Results with smooth surface condition. For  $x > 0$  there is a vacuum, for  $x < 0$  solid steel. Right: Results with rough surface condition. The red line correspondent to the steel density varies due to the sinusoidal surface roughness. From a depth of  $\approx 60$  nm, the material is completely solid.

figures 4.3. It is easy to see with the eye that the mean implantation depth increases as well as a smearing of the distribution takes place. The parameters to quantify this behaviour are the mean value and the variance. In table A.1 all characteristic values are listed. The first visual impression is confirmed. In case of a smooth surface the average implantation depth increases from 8.42 nm to 19.00 nm. In the same area the variance has increased by 119%. It should be noted that the number of implemented particles decreases slightly along the decay series, since some of the daughter nuclei leave the spectrometer wall due their recoil energy. The decrease is also shown in table A.1 in appendix. Visually this behaviour can be seen well in the scatter plots 4.4.

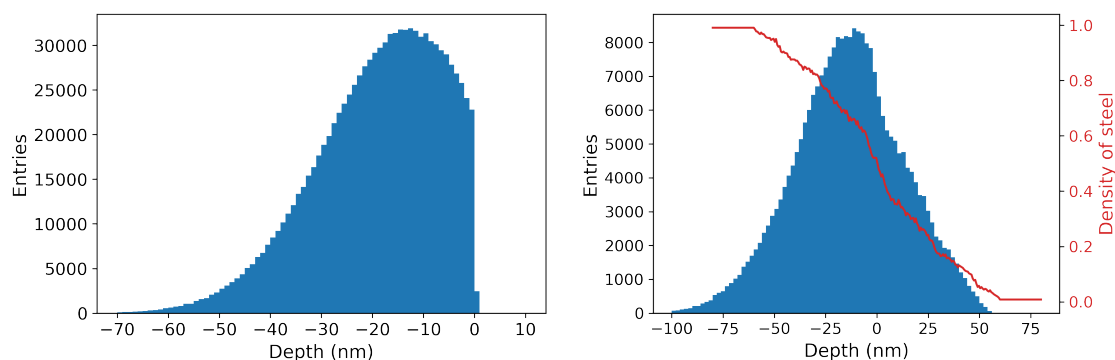


Figure 4.3.: Change of implantation depth along the decay chain Left: Result with a smooth surface. For  $x > 0$  there is a vacuum, for  $x < 0$  solid steel. Right: Result with rough surface. The red line correspondent to the steel density varies due to the sinusoidal surface roughness. From a depth of  $\approx 60$  nm, the material is completely solid.

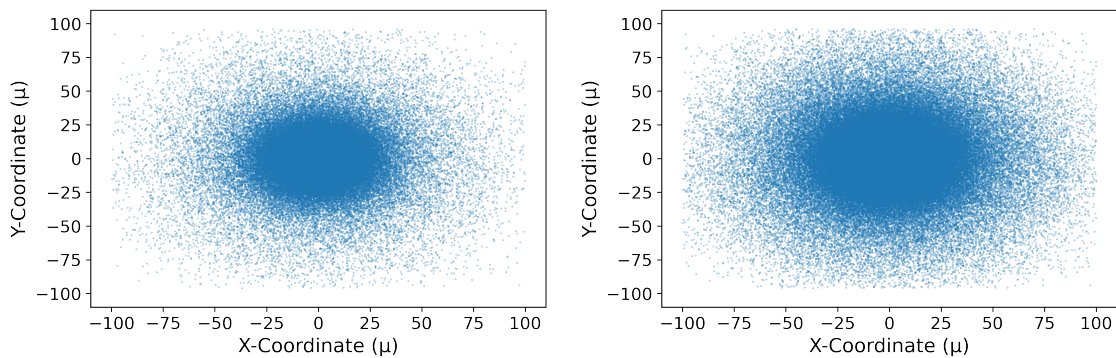


Figure 4.4.: Scatter plots along the decay chain with smooth surface. The number of implanted particles is decreasing along the decay chain. Left: Each point represents an implanted  $^{210}\text{Pb}$  atom. Right: Each point stands for an implanted  $^{218}\text{Po}$  atom.

### 4.3. $^{210}\text{Pb}$ Decay

The actual sputtering analysis begins with the decay of  $^{210}\text{Pb}$ . This  $\beta$  emitter has a half-life of 22.2 years [71] and is by far the most long-lived element of the observed decay series. Therefore  $^{210}\text{Pb}$  has accumulated in the spectrometer wall and is still present there today. For a complete sputtering analysis an extension of the simulation is necessary at this point. Although an ultra high vacuum with  $\sim 10^{-11}$  mbar is realised by TMP and NEG pumps, as described in chapter 2.2, there is always residual gas in the spectrometer. This residual gas consists essentially of  $\text{H}_2\text{O}$  and  $\text{H}_2$  [72]. Since it is energetically more favourable for residual gas atoms to bind to the surface, an additional layer of water and hydrogen accumulates there. These atoms can also be sputtered and must therefore be considered as an additional boundary layer in the simulation.

The exact amount of atoms bonded to the surface is unknown, so the standard simulation assumes 30% of a mono layer of hydrogen. This is realised by implementing a hydrogen gas in a 3 nm thick layer above the surface. A Van-der-Waals bond between gas and surface does not exist as it would be the case with physical adsorption. A small parameter study varies the proportion of hydrogen atoms to simulate up to three hundred mono layers.

To calculate the number of atoms per mono layer of hydrogen, a covalent bond between the hydrogen atoms is assumed, which corresponds to a molecule size of 75 pm [73]. So per  $\text{cm}^2$  about  $7.1 \cdot 10^{16}$  hydrogen atoms are present. The same analysis is made with water as additional surface layer. To calculate the mean distance of the water molecules the rule of three is used on the basis of molecular water mass and avogadro constant. The result is about 0.31 nm which corresponded with  $1.04 \cdot 10^{15}$  molecules per  $\text{cm}^2$ . The effects on the sputter yield with smooth surface condition are summarised in figure 4.5.

The graphs are focused on the sputter yield with respect to the steel particles and the boundary layer particles. With minimal boundary layer, as expected, there is no difference in the number of sputtered steel particles because the influence of the boundary layer is negligible. The extent of the sputtered surface layer particles differs in the respective maximum by a factor of 4. This can be qualitatively explained by the ionisation rate and elastic scattering cross sections. According to the non-relativistic Bloch formula for

ionisation losses of ions in matter, the energy loss per unit distance is proportional to the electron density and mean excitation energy of matter, see formula 4.2 where  $n$  is the electron density and  $I$  the mean excitation energy of matter.

$$-\frac{dE}{dx} = \frac{4\pi n z^2}{m_e v^2} \cdot \left(\frac{e^2}{4\pi\epsilon_0}\right)^2 \cdot \ln\left(\frac{2m_e v^2}{I}\right) \quad (4.2)$$

Since the packing density of the hydrogen layer is about 17 times higher than that of water, but the water layer has an electron density 18 times higher, the differences in ionisation losses can be calculated through  $I$ . The mean excitation energy of water is 78 eV [61] and therefore 3.8 times higher than of hydrogen [74]. This results in a higher ionisation rate in the water layer depending on velocity. In comparison of the two boundary layers, however, also a difference in the elastic cross section can be observed. According to electron scattering experiments, the elastic cross section of water with  $3.42 \cdot 10^{-16} \text{ cm}^2$  is about 4.6 times higher at 100 eV as at molecular hydrogen and is almost equal to inelastic cross section [75, 76]. This differs strongly to hydrogen where the inelastic cross section is 2.4 times higher as the elastic one. Therefore, the steel particles in the water boundary layer lose energy faster through scattering than of ionisation compared to the hydrogen layer. This explains the higher number of sputtered boundary layer particles into the inside of the spectrometer in case of water layer. Furthermore the steel and boundary yield decreases faster because the energy losses due to scattering and ionisation are higher. The influence of the boundary layer on the sputter yield is therefore proven. A quantitative simulation taking into account surface effects would be the next step, but this cannot be simulated within the framework of the physics list used.

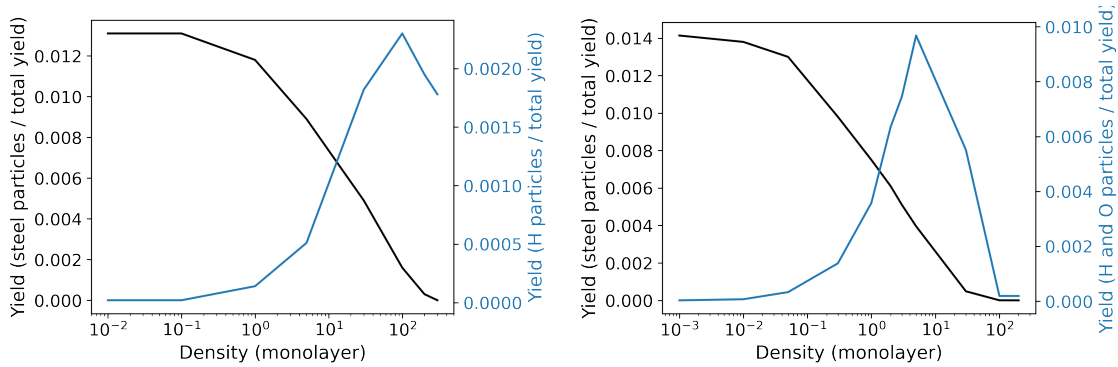


Figure 4.5.: Parameter study: Density variation of hydrogen (left) and water (right) layer. The sputter yield of steel and boundary particles are given as a dependency of the density of the film. A distinction is made between different yields. All results are with smooth surface conditions and at least one million particle decays per density are simulated.

The central results are summarised in Figure 4.8. Further figures are for completeness in appendix A.3. The angular  $\phi$  distribution shows small differences between rough and smooth surfaces. The valleys and peaks of the periodic valley mountain structure are aligned parallel to the  $y$ -axis. This helps to explain the local suppression of the  $\phi$

sputter angles at  $\pm\pi/2$ . A particle sputtered in a valley is more likely to hit the surface again if the  $\phi$  direction points to a mountain. In this case a reimplantation and thus suppression is possible. On top of that there exist an implantation systematic. During the implantation process, all particles originate from an area of origin that is small in relation to the surface area, as described in 4.1. Thus the source can be roughly seen as a point source if the distance to the source area is more than  $4\ \mu\text{m}$  which applies to one third of all particles. Therefore there exists a no homogeneous implantation fraction on the surface. The mountain-valley structure gets the property of a sun and shadow side, whereby only the sun side is bombarded with particles. The effect of the systemic approach can be seen in figure 4.6. The result is a suppression of the  $\phi$  angle in the direction of the shadow side. The total effect of  $\phi$  suppression is less then 5% compared to smooth surface condition.

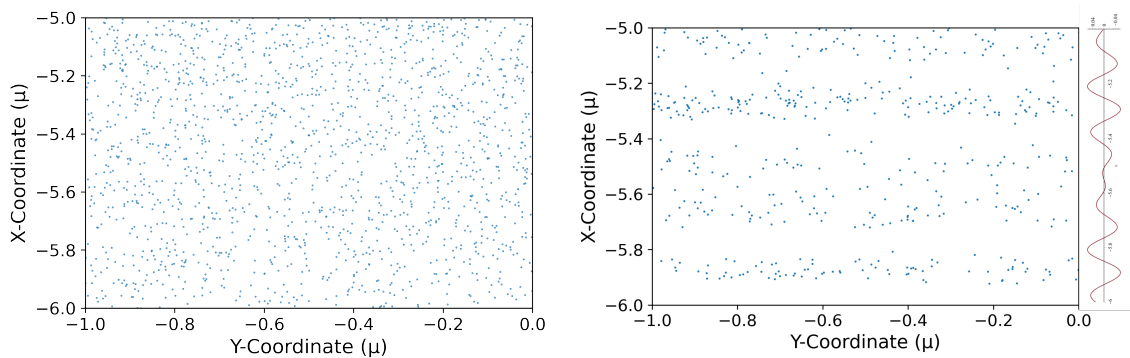


Figure 4.6.: Implantation systematic Left: At smooth surface condition a homogeneous implantation can be observed. Right: At rough surface condition only on sun side of the mountain-valley structure events can be registered. The periodic change of surface is plotted next to the figure.

In chapter 2.4 the dependence of the sputter yield on the  $\Theta$  angle is discussed. Due to the fact that ions are the projectile particles no cosine distribution is to be expected. In figure 4.7 instead a mass dependent peak at about  $43\text{--}46^\circ$  is observed. This corresponds to the expected behaviour in terms of quality and corresponds quantitatively to the SRIM result of Hinz [8]. However, the angular distribution of the alpha nuclei follows almost perfectly a cosine function. This is due to the fact that the nuclei with MeV energy hardly interact in the short distance with the material. Therefore the distribution corresponds to the expected isotropic decay distribution.

The energy distributions hardly differ between smooth and rough surfaces. In the electron spectrum, the convergence peaks of  $^{210}\text{Pb}$  [71] at 30.1 keV and 42.5 keV are clearly visible. This is in agreement with the measurements of Harms[6], which suggests the observation of conversion electrons in the main spectrometer. In both surface configurations, electrons are the most commonly sputtered particles. In addition,  $^{206}\text{Pb}$  and alpha nuclei occur relatively often. Almost three of four sputtered ions are iron ions. This corresponds to the mass ratio in the used steel. In contrast to SRIM, it is currently not possible in Geant4 to track the ion energy down to the sub-eV energy range. Instead, at 1 keV at the latest, all residual energy is deposited in the surrounding material [65]. Therefore a sputtering

energy analysis according to the equation 2.15 is not possible. SRIM results for neutral particles in this respect can be found in the work of Hinz [8].

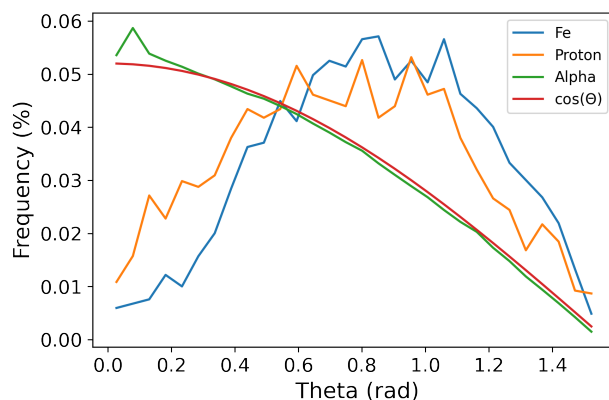


Figure 4.7.: Theta distribution of different sputtered species with smooth surface condition. The angular distribution of the sputtered ions differs greatly from the cosine distribution. The alpha distribution corresponds to the isotropic decay distribution.

#### 4.4. Impact of sputtering

The main focus of the analysis of the effects of sputtering are the ions released after chapter 4.3. From the theoretical descriptions in chapter 2.3.2 it is clear that the current background in the main spectrometer is mainly caused by uncorrelated, spatially homogeneously distributed and low energy electron production mechanisms. The spatial homogeneity of the background implies electrically neutral production mechanisms. This leads to the idea that the excited sputter ions neutralise themselves by capturing an electron. This allows free propagation in the spectrometer. Subsequent ionisation by means of black body radiation or similar can produce low-energy electrons. The probability for this process is to be qualitatively estimated in the following. Simplifying assumptions are made for this. For example, the effective cross section should be the same for all ions. Electrons which are produced during decay should be in the spectrometer volume at the same time as the ions. Finally, the B- and E-fields are homogeneous because only the area between spectrometer wall and inner electrode is considered.

The probability for the capture of an electron is calculated with

$$P = \sigma \frac{N}{A}, \quad (4.3)$$

where  $\sigma$  is the cross section,  $N$  is the number of electrons and  $A$  is the cross-sectional area of the projectile beam. The cross section is assumed to be energy independent and is  $5 \cdot 10^{-16} \text{ cm}^2$  [77]. The number of electrons is calculated from two components. The first part results from sputtering, according to Figure 4.9 about 0.034 electrons can be assumed. It is important to note that only  $^{210}\text{Po}$ -electrons are considered here because of the temporal

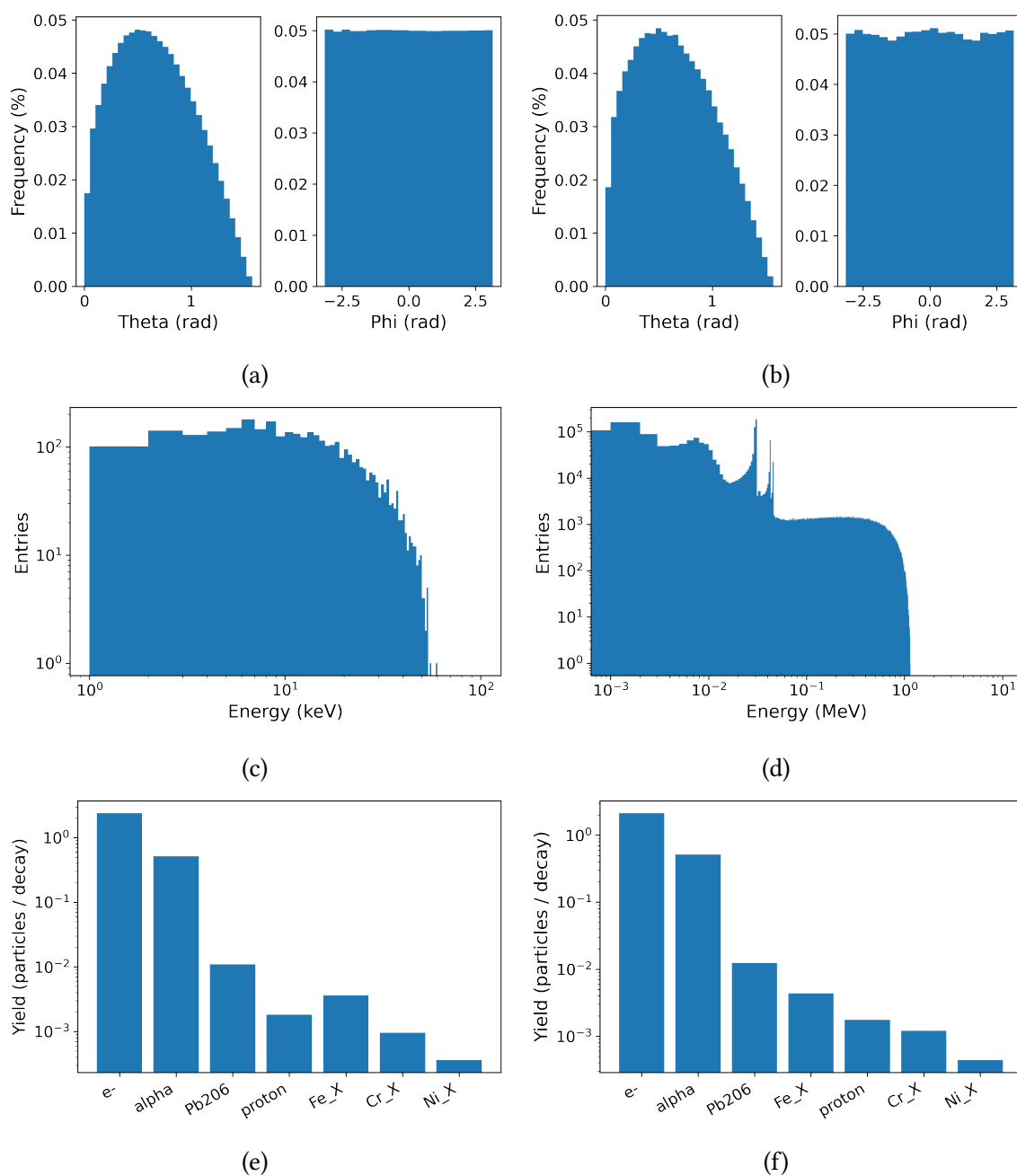


Figure 4.8.: Results sputter analysis: **(a)**: Angular distribution of all sputtered particles for a smooth surface. The  $\phi$  angle is uniform distributed while  $\Theta$  distribution has a local maximum is at  $\approx 31^\circ$ . **(b)**: Due to the surface structure a different  $\phi$  angular distribution can be observed in rough surface cases, see text.  $\Theta$  distributions do not differ from smooth surface. **(c)**: Energy distribution of all iron isotopes, smooth surface **(d)**: Energy distribution of electrons, smooth surface **(e)**: Sputter yield broken down by particle type, smooth surface **(f)**: Sputter yield broken down by particle type, rough surface

relationship. The second fraction is the electrons emitted from the spectrometer wall independently of the sputtering. It can be assumed that about 18 electrons are emitted per  $m^2s$  [78]. Since these are accelerated back to the spectrometer wall by the E-field of the inner electrode, these particles remain on average far below one  $\mu s$  in the spectrometer volume. Therefore, their probability density is too low to have an influence on the probability of capture. There is a third electron component which is located inside the flux tube volume. However, as this estimation is limited to the area between spectrometer wall and inner electrode it will not be considered in the following calculations. The basis for the construction of the cross-sectional area is the trajectory of the electrons. Due to the E- and B-field approximation, neither the trajectory of the electrons nor that of the ions can be calculated exactly within the scope of this estimation. However, an upper limit for the radius  $R$  of the electron orbit can be determined. In the following, it is assumed that the circular area  $A$ , which is spanned by the radius  $R$ , forms the base of the cylinder in which the electron is located with equally distributed probability. Thus the radius  $R$  is the only unknown quantity. The calculation is done by solving the equations of motion of a charged particle in the E- and B-field. According to Lorentz applies:

$$\vec{F} = q\vec{v} \times \vec{B} + \vec{E}q \quad (4.4)$$

$$m \begin{bmatrix} \ddot{x} \\ \ddot{y} \\ \ddot{z} \end{bmatrix} = q \begin{bmatrix} -\dot{z}a \\ 0 \\ \dot{x}a \end{bmatrix} + q \begin{bmatrix} -b \\ 0 \\ 0 \end{bmatrix} \quad (4.5)$$

where  $a$  is the magnetic field strength and  $b$  is the E-field strength. At the spectrometer wall, the magnetic field strength in the standard configuration is 6.3 G and the E-field is  $1333 \frac{V}{m}$  strong[37]. To assume these values as constant is justified by the fact that the neutralisation of the ions should take near to the spectrometer surface.

The solution of the equation 4.5 is done numerically using the odeint function of the scipy package of Python. The velocity components of the electrons are calculated from the energy and the exit angle of the electrons from the spectrometer surface, which are defined by the distributions in Figure 4.8, see equation 4.6.

$$v_x = \sqrt{\frac{2 \cdot E \cos(\phi) \sin(\theta)}{m}}, \quad v_y = \sqrt{\frac{2 \cdot E \sin(\phi) \sin(\theta)}{m}}, \quad v_z = \sqrt{\frac{2 \cdot E \cos(\theta)}{m}} \quad (4.6)$$

The boundary conditions of the ODE are created by randomly picking energy and exit angles from the respective distributions. Frequent repetition of this process leads to a radius distribution, see figure 4.9, which enables a probability estimation according to the equation 4.3.

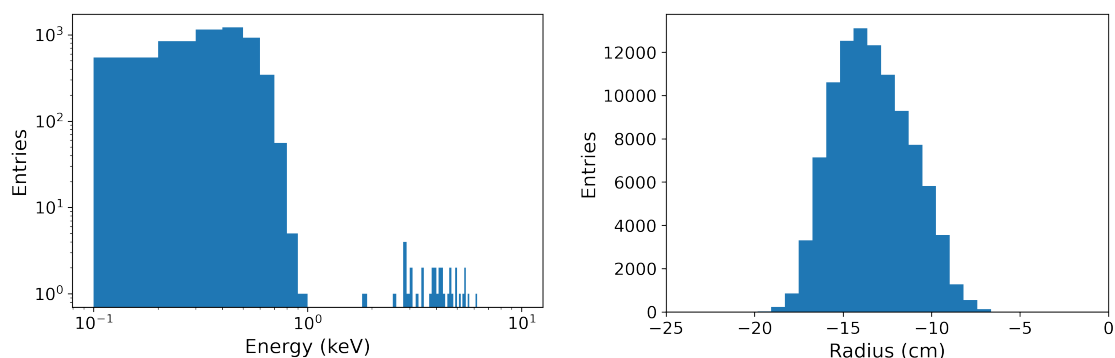


Figure 4.9.: Left: Energy distribution of electrons only at  $^{210}\text{Po}$  decay, smooth surface condition. Right: Simulated radius distribution of 100000 sputtered electrons.

The probability of at least one event per hour to be observed is  $8.3 \cdot 10^{-12}$ . Thus it is obvious that this production path is negligible for further background studies. As the simplifications of the estimations tend to lead to an overestimation of this production path, an even smaller result can be expected with an exact calculation by means of KASSIOPEIA<sup>3</sup>. Even the addition of the third not considered electron component would not significantly increase the probability. This would require an electron density several orders of magnitude higher than near the spectrometer surface.

<sup>3</sup>Customised simulation package for the KATRIN Experiment. It includes detailed E- and B-field information about KATRIN and more, see [79]



## 5. Tritium analysis

The following chapter deals with the tritium contamination of the spectrometer section, which took place on 09.12.2019. As the original design report [5] already shows, tritium in the main spectrometer (MS) corresponds to the worst case scenario of the operative operation. By opening a valve of the Forward Beam Monitor (FBM) [37] section, a pressure increase in the CPS occurred. Due to the pressure difference, a particle flow started from the FBM through CPS and PS into the MS, with a significant effect on the background rate. Compared to the KNM2  $\beta$  measurements, this has increased from  $0.211 \pm 0.004$  cps to about  $1.75 \pm 0.07$  cps. The increased background is due to tritium in the main spectrometer. It is present in either HT or HTO form. This chapter is intended to describe the effect of tritium on the background and discuss the time evolution of the contamination.

### Contamination progress

The effect of the contamination on the background can be well illustrated by radial plots of different time intervals. In figure 5.1 the data from KNM2 and from the first month after the contamination event are plotted. Due to the tritium in the spectrometer, an inversion of the typical radial plot can be determined in addition to a background increased by the factor 8.3. The inversion is due to an electron cascade starting from the primary tritium electrons. These high-energy particles generate further low-energy secondary electrons by impact with the residual gas. By iterative repetition the energy decreases steadily until the trapping condition is broken and the secondary electrons can reach the detector. This tends to happen at low energies, which increasingly hit the inner detector area. This connection is due to the radial drift of the electrons. In principle, due to the axially symmetric fields in the spectrometer, no radial drift is possible because of the conservation of angular momentum [5]. But this does not apply in the presence of small disturbances of the axial symmetry, as it is the case in the MS [5]. Particles with low azimuthal magneton drift velocity experience this effect most strongly [80]. Since azimuthal motion depends on kinetic energy, low-energy particles are particularly affected by radial drift. Therefore, there are more events in the inner flux tube volume due to tritium contamination, as shown in figure 5.1.

At the moment the valve was opened, the PS and MS were flooded with tritium molecules from the FBM section. The characteristic pump-down time  $\tau_p$  describes the speed of flooding of two volumes of different pressure. This depends on the effective pumping speed  $S_{\text{eff}}$ , which is calculated by

$$\frac{1}{S_{\text{eff}}} = \frac{1}{S} + \frac{1}{C}. \quad (5.1)$$

## 5. Tritium analysis

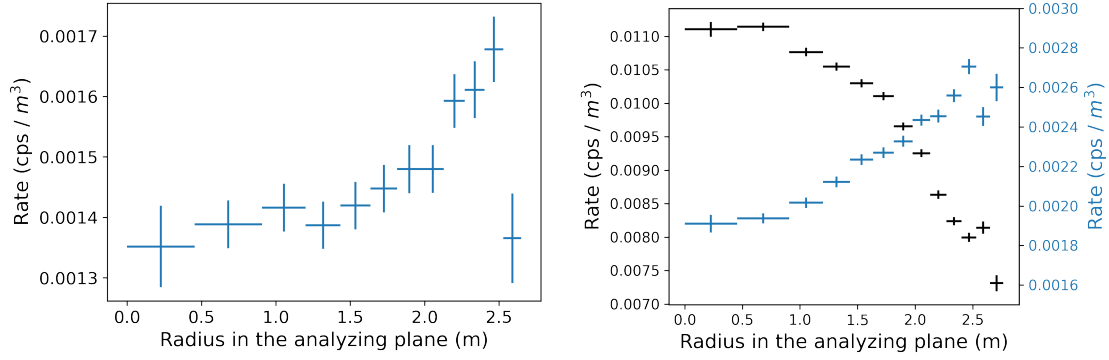


Figure 5.1.: Background Rates over radius of analysing plane. All rates are normalised to sensitive volume. Left: The data are taken from the KNM2 period 2 data set, see table A.3 for run numbers. Rate on last ring is lower because of pixel shadowing. Right: Black corresponds to the first 36.6 hours after the contamination event and blue to the time interval from 654.4 to 686.4 hours.

Here  $S$  corresponds to the pumping speed and  $C$  to the conductance of the connecting pipeline section [81] of the considered volumes. The pumping speed is dominated by the particle type dependent absorption capacity of the getter pumps and the copper baffles. The change in pressure is determined in the first seconds by the flooding and is calculated using the formula 5.2 [82]. Here  $\tau_p$  is approximately 7 s large [81]. After this period of time the pressure from the tritium molecules sticking to the surface is dominant. If this is tritium of the HT form, it would mainly stick to getter pumps [81]. With HTO, an accumulation of cryogenic baffles would be observed instead [81]. A further change in pressure is now due to a reduction of the adsorbed particles on the surface. This is determined by the sojourn time  $\tau_S$ , which depends on the desorption enthalpy, see equation 5.3.

$$p(t) = p_0 + p_1 \cdot e^{-t/\tau_p} \quad (5.2)$$

$$\tau_S = \tau_0 e^{\frac{E_H}{k_B T}} \quad (5.3)$$

In summary, it can be said that the background reduction is accompanied by the detachment of the tritium molecules from the spectrometer wall. The effective average bonding time for this process results from the superposition of several functions according to the formula 5.3. For the theoretical calculation the knowledge of the substance and surface dependent desorption enthalpy would be necessary. For the practical calculation, only an exponential fit over the temporal course has to be carried out. In figure 5.2 the temporal course of the first 686.4 h hours after the contamination event is shown. The following measurement conditions and restrictions apply to the data on which the plot is based.

The hours 208.2 to 262.4 are not taken into account, because in this time interval the getter pumps have been heated to 30 °C. The counter voltage was always at k35<sup>1</sup>>18573 V, as for the background signal during tritium measurement campaigns. The entire measurement campaign is carried out under increased argon pressure of 0.84 – 3.0 · 10<sup>-8</sup> mbar and by

<sup>1</sup>k35 is the name of the custom-made ppm-precision high voltage divider, which measures the retarding potential [37]

means of a special electrode configuration, which approximately doubles the effective flux tube volume. Also some detector pixels are not considered when creating the plots. Pixelcuts are a standard procedure used to obtain high quality data at the expense of statistical data. There are two main reasons for performing a cut. Firstly, the pixels are defective, which in this case results in a distorted energy resolution compared to the other pixels. Secondly, due to shadowing by beamtube parts the pixels show less or more statistics on a time average, which contradicts the assumption that a homogeneous event distribution on the detector is to be expected. The numbers of the excluded pixels can be taken from A.2. At this point it should be noted that the measured background is not directly comparable with previous measurements. Therefore a normalisation to the new sensitive volume must be carried out. The run number list can be found in appendix A.4 . Overall, the background decreases exponentially in the time interval considered, with a half-life of 132.7 h. The rapid decrease shows the effectiveness of the pumping performance. It can be stated that even in the worst case no lasting impairment of the KATRIN experiment can be observed. The careful and robust construction of the KATRIN experiment is particularly evident in this case. The temporal consideration according to figure 5.2 is

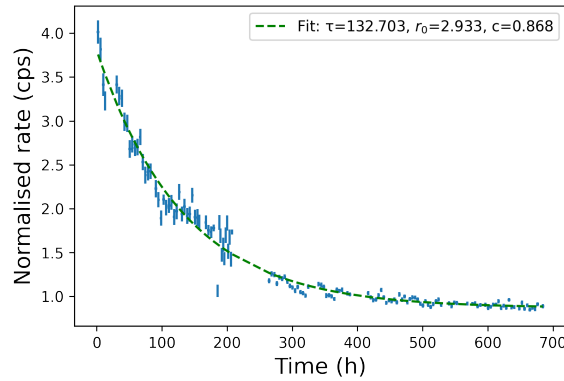


Figure 5.2.: Total background rate over time. The high background rate of tritium contamination decreases in the first  $\approx 700$  h according to an exponential function. The uncertainty bars are taken from Kaehm’s analysis [83].

also applicable to each ring individually, see figures A.7 and A.8. When plotting the ring resolved temporal background course, a pixel cut according to table A.2 is also carried out and only data with  $k35 > 18573$  V are used. Here it is clearly visible that the inner rings show an exponential decrease during whole observation time, while the outer rings also show an exponential decrease but they converged to a constant value from hour 300, see figure 5.3. This behaviour is in line with the expectation because the additional tritium background is projected disproportionately onto the inner rings. Thus the exponential decrease in this area lasts longer until a levelling out around a constant value occurs.

In addition to the time-dependent view of the total background rate, it is possible to display the background in a radial profile at different time intervals. This corresponds to a spatial variation in discrete time steps. For this purpose, the background rate is standardised to the first 208 hours of contamination. This means that the background is

## 5. Tritium analysis

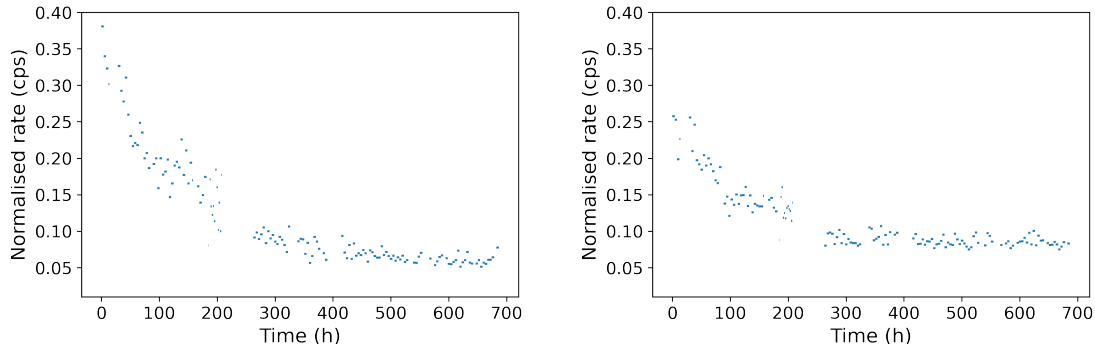


Figure 5.3.: Background Rates over time per ring. Each data point represent the background rate of one run. Normalised to effective pixel number, see table A.2. Left: Background of the ring number two. Right: Background of the outermost ring.

given in % of the highest contamination. The result for the selected data sets is shown in figure 5.4. The time intervals used correspond to the data sets KNM3a, KNM2Period2 and TritiumContamination see A.3 and A.4. It can be clearly seen that the background during contamination is much higher then ever before. Furthermore, the effect on the background can be seen through the SAP<sup>2</sup> setting. The KNM3a background rate with SAP setting is reduced by about 31% compared to the KNM2Period2 data set. The positive effect on the background regarding the reduction of the effective flux tube volume is in accordance with the knowledge gained from the dependence on the B-field according to chapter 2.3.2. This shows that the previous understanding of the remaining KATRIN background is in agreement with the experimental results.

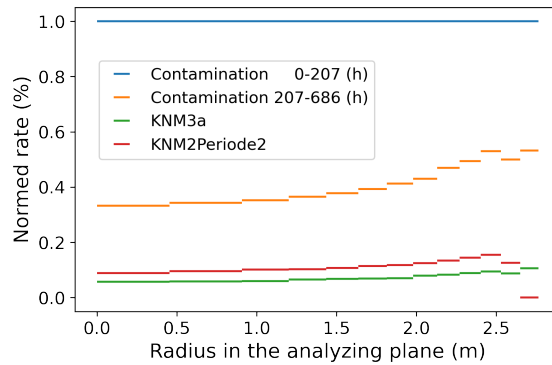


Figure 5.4.: Normalised background rates of different data sets over radius of the analysing plane. The normalised background rate of the orange data set is about twice as high as in the red data set because twice as much flux volume is observed. The KNM3a background rate is the lowest due the SAP setting.

<sup>2</sup>Shifted Analysing Plane - Field configuration to reduce effective flux tube volume, see [84].

## 6. Conclusion

In the course of the contamination analysis it can be stated that the worst case scenario of the operational process does not cause lasting problems. The behaviour of the tritium molecules under the experimental parameters pressure and temperature follows the predictions. Thus, the experimental know-how of KATRIN Collaboration enables reliable measurements even under the most difficult conditions.

The declared goal of the KATRIN experiment is to determine the electron antineutrino mass with an accuracy of  $200 \text{ meV}/c^2$ . One of the design criteria for achieving this goal is a background rate of 10 mcps. This rate is currently exceeded by a factor of about thirty. Therefore, concerning the fulfilment of the target, it is of particular interest to understand the background in detail in order to be able to carry out a reduction as efficiently as possible. Earlier measurements show that a high  $^{210}\text{Pb}$  activity prevails inside the main spectrometer. This leads to the development of the Rydberg underground model. The central generation mechanism is the sputtering occurring through radioactive decays from  $^{210}\text{Pb}$  via  $^{210}\text{Po}$  to  $^{206}\text{Pb}$ . Here, electrically neutral and charged particles, some of them highly excited, enter the interior of the spectrometer. If the particles are highly excited they are called Rydberg atoms, which can be ionised by the BBR for example. Since ions receive additional kinetic energy due to the electric field, they can fulfil the homogeneity condition of the background even with a short lifetime. However, the basic requirement is the neutralisation of the ions to capture electrons in higher lying states. For the calculation of the probability of the ion based background production path, a Geant4 sputtering simulation has been created within the scope of this thesis. The probability estimation based on the simulation results shows that the investigated production mechanism is very unlikely. In one hour observation time the probability to observe at least one ion neutralisation between spectrometer surface and inner electrode is about  $8.3 \cdot 10^{-12}$ . The reason is the low electron density near the spectrometer surface. A further detailed investigation is therefore not promising. However, two possible simulation extensions should be mentioned at this point. Firstly, the inner spectrometer surface is surrounded by an oxide layer, therefore a modification of the steel used in the peripheral area is useful. This would have a great influence on the sputtered ion composition, especially more oxygen would be sputtered. In this context, the surface coating with water and hydrogen by adhesion can be considered. Currently, the surface coating is simulated by a gas layer. Furthermore, the effects of the sputtered particles on the background have only been considered qualitatively in an estimation. Integration into a KASSIOPEIA simulation would allow a quantitative analysis under consideration of real E- and B-field configurations and the electrons inside the flux tube could be taken into account. Nevertheless, sputtered ions do not contribute as a dominant part of the background.

Further investigations will be necessary for the future to create a complete background model. For example, a complete sputtering simulation is desirable. In addition to yield

and angular distribution, this simulation should include the excitation energy of the sputtered particles. A further project is investigating the temporal influence of the BBR on the Rydberg atoms. The basic idea is that low-energy Rydberg atoms can reach higher energetic states on average over time by iterative excitation using BBR [85]. This could motivate the necessary lifetime of the Rydberg atoms. A theoretical possibility for Rydberg background reduction would be the installation of an infrared LASER. This would be tuned to the energy of specific Rydberg states and would be able to de-excite them by stimulated emission before they are ionised. The technical sticking point would be the heat generated by the LASER and the associated heating of the main spectrometer. Thus, the theoretical investigation of the background as well as the practical reduction remains an exciting part of the KATRIN experiment.

# Bibliography

- [1] W. Pauli. *Offener Brief an die Gruppe der Radioaktiven bei der Gauverein-Tagung zu Tübingen*. [Online]. Available: [https://cds.cern.ch/record/83282/files/meitner\\_0393.pdf](https://cds.cern.ch/record/83282/files/meitner_0393.pdf) [Access on: 08.09.2020]. 1930.
- [2] Cowan C. et al. "Detection of the Free Neutrino: a Confirmation". In: *Science*, Vol. 124, Issue 3212 (1956).
- [3] C. Walter. "The Super-Kamiokande Experiment". In: *arXiv*, arXiv:0802.1041 (2008).
- [4] A. Osipowicz et al. "Letter of Intent". In: *Los Alamos e-print archive* (2001).
- [5] KATRIN Collaboration. "KATRIN Design Report". In: (2004).
- [6] F. Harms. "Characterization and Minimization of Background Processes in the KATRIN Main Spectrometer". PhD thesis. Karlsruher Institut für Technologie (KIT), 2015.
- [7] N.Trost. "Modeling and measurement of Rydberg-State mediated Background at the KATRIN Main Spectrometer". PhD thesis. Karlsruher Institut für Technologie (KIT), 2018.
- [8] D. Hinz. "Ionisation mechanisms of  $^{206}\text{Pb}$  induced Rydberg atoms". MA thesis. Karlsruher Institut für Technologie (KIT), 2018.
- [9] Musée Curie. *Cowan and Reines*. [Online]. Available: [https://www.radioactivity.eu.com/site/pages/Neutrino\\_Discovery.htm](https://www.radioactivity.eu.com/site/pages/Neutrino_Discovery.htm) [Access on: 08.09.2020].
- [10] L. Oberauer. *Neutrino Physik Grundlagen Experimente und aktuelle Forschung*. Springer Spektrum, 2019. DOI: <https://doi.org/10.1007/978-3-662-59335-6>.
- [11] The DONuT Collaboration. "Final tau-neutrino results from the DONuT experiment". In: (2007). DOI: [10.1103/PhysRevD.78.052002](https://doi.org/10.1103/PhysRevD.78.052002).
- [12] B. Povh et al. *Teilchen und Kerne eine Einführung in die physikalischen Konzepte*. Springer Spektrum, 2014. DOI: [DOI10.1007/978-3-642-37822-5](https://doi.org/10.1007/978-3-642-37822-5).
- [13] MissMJ. *Standard model of elementary particles: the 12 fundamental fermions and 5 fundamental bosons*. [Online]. Available: [https://en.wikipedia.org/wiki/Elementary\\_particle#/media/File:Standard\\_Model\\_of\\_Elementary\\_Particles.svg](https://en.wikipedia.org/wiki/Elementary_particle#/media/File:Standard_Model_of_Elementary_Particles.svg) [Access on: 05.11.2020].
- [14] R. Holanda et al. "An estimate of the dark matter density from galaxy clusters and supernovae data". In: *arXiv:1905.09689* (2019).
- [15] W. Haxton. "THE SOLAR NEUTRINO PROBLEM". In: *arXiv:hep-ph/9503430* (1995).

- [16] SNO Collaboration. “Direct Evidence for Neutrino Flavor Transformation from Neutral-Current Interactions in the Sudbury Neutrino Observatory”. In: *Phys. Rev. Lett.* volume 89, No. 1, 011301 (2002).
- [17] P. Wildenhain, K. Landea. “The Homestake Chlorine Solar Neutrino Experiment—Past, Present and Future”. In: *Nuclear Physics B (Proc. Suppl.)* 118 (2003) 49-54 (2003).
- [18] A. Suzuki. *Historical Account*. In: Fukugita M., Suzuki A. (eds) *Physics and Astrophysics of Neutrinos*. Springer, Tokyo, 1994. DOI: [http://doi.org/10.1007/978-4-431-67029-2\\_3](http://doi.org/10.1007/978-4-431-67029-2_3).
- [19] Super-Kamiokande Collaboration. “A Measurement of Atmospheric Neutrino Oscillation Parameters by Super-Kamiokande I”. In: *arXiv, arXiv:hep-ex/0501064* (2005).
- [20] The Royal Swedish Academy of Sciences. *The Nobel Prize in Physics 2015*. [Online]. Available: <https://www.nobelprize.org/uploads/2018/06/press-30.pdf> [Access on: 05.11.2020].
- [21] H. Hanser et al. “Neutrinos - Die mysteriösen Geisterteilchen weisen den Weg zu einer neuen Physik”. In: *Spektrum der Wissenschaft* (2013).
- [22] KamLAND Collaboration. “Measurement of Neutrino Oscillation with KamLAND: Evidence of Spectral Distortion”. In: *Physical Review Letters* (2005). DOI: 10.1103/PhysRevLett.94.081801.
- [23] C. Zhang, P. Vogel, L. Wen. “A Neutrino oscillation studies with reactors”. In: *Nature* (2015). DOI: 10.1038/ncomms7935.
- [24] M. Agostini et al. “Improved limit on neutrinoless double beta decay of  $^{76}\text{Ge}$  from GERDA Phase II”. In: *arXiv:1803.11100* (2018).
- [25] JabberWok2. *Feynman Diagram of double beta decay*. [Online]. Available: [https://upload.wikimedia.org/wikipedia/commons/3/34/Double\\_beta\\_decay\\_feynman.svg](https://upload.wikimedia.org/wikipedia/commons/3/34/Double_beta_decay_feynman.svg) [Access on: 07.09.2020].
- [26] GERDA Collaboration. *The GERmanium Detector Array*. [Online]. Available: <https://www.mpi-hd.mpg.de/gerda/> [Access on: 07.09.2020].
- [27] J. Loredano, Q. Lamb. “Bayesian analysis of neutrinos observed from supernova SN 1987A”. In: *arXiv:astro-ph/0107260* (2001).
- [28] Planck Collaboration. “Planck2013 results. XVI. Cosmological parameters”. In: *arXiv*: (2014).
- [29] C. Weinheimer et al. “The Mainz Neutrino Mass Experiment”. In: *International Europhysics Conference on HEP* (2001).
- [30] KATRIN Collaboration. “An improved upper limit on the neutrino mass from a direct kinematic method by KATRIN”. In: *Phys. Rev. Lett.* 123, 221802 (2019).
- [31] A. Nucciotti et al. “Status of the HOLMES experiment to directly measure the neutrino mass”. In: *Journal of Low Temperature Physics* (2018).
- [32] S. Rupp. “Development of a highly sensitive hollow wave guide based Raman system for the compositional analysis of the KATRIN tritium source gas”. PhD thesis. Karlsruher Institut für Technologie (KIT), 2016.

- 
- [33] C. Weinheimer. “KATRIN, a Next Generation Tritium  $\beta$  Decay Experiment in Search for the Absolute Neutrino Mass Scale ”. In: *Progress in Particle and Nuclear Physics* 48 (2002).
- [34] C. Vaissière et al. *Tritium, A radioactive isotope of hydrogen*. [Online]. Available: <https://www.radioactivity.eu.com/site/pages/Tritium.html> [Access on: 09.10.2020].
- [35] PNGWing. *KATRIN Tritium Beta decay*. [Online]. Available: <https://www.pngwing.com/en/free-png-smzvy> [Access on: 19.10.2020].
- [36] Inductiveload. *Beta-minus Decay*. wikimedia [Online]. Available: [https://commons.wikimedia.org/wiki/File:Beta-minus\\_Decay.svg](https://commons.wikimedia.org/wiki/File:Beta-minus_Decay.svg) [Access on: 27.07.2020].
- [37] KATRIN Collaboration ; soon be published. “The KATRIN Experiment for the measurement of the absolute mass scale of neutrinos”. In: ().
- [38] KATRIN Kollaboration. *The Differential Pumping Section*. [Online]. Available: <https://www.katrin.kit.edu/304.php> [Access on: 28.07.2020].
- [39] G. Beamson et al. “The collimating and magnifying properties of a superconducting field photoelectron spectrometer ”. In: *J. Phys. E: Sci. Instrum.* 13 64 (1980).
- [40] M. Leung. “The Borexino Solar Neutrino Experiment: Scintillator Purification and Surface Contamination ”. PhD thesis. Princeton University, 2006.
- [41] F. Fränkle et al. “Radon induced background processes in the KATRIN pre-spectrometer ”. In: *Astroparticle Physics* 35 128-134 (2011).
- [42] F. Harms J. Wolf. “Simulation and measurement of the suppression of radon induced background in the KATRIN experiment ”. In: *AIP Conference Proceedings* (2018).
- [43] F. Müller. “Efficiency Studies of the Background Suppression by a Liquid-Nitrogen Cooled Baffle System in the KATRIN Experiment ”. MA thesis. Karlsruher Institut für Technologie (KIT), 2015.
- [44] F. Fränkle et al. “Radon induced background processes in the KATRIN pre-spectrometer ”. In: *arXiv:1103.6238v1* (2011).
- [45] C. Grupen. *Grundkurs Strahlenschutz, Praxiswissen für den Umgang mit radioaktiven Stoffen*. Springer Spektrum, 2014.
- [46] United States Environmental Protection Agency. *Radon*. [Online]. Available: <http://www.epa.gov/radiation/radionuclides/radon.html> [Access on: 12.10.2020].
- [47] Tosaka. *Decay chain(4n+2, Uranium series)*. Wikimedia [Online]. Available: [http://commons.wikimedia.org/wiki/File:Decaychain%284n+2,Uranium series%29.PNG](http://commons.wikimedia.org/wiki/File:Decaychain%284n+2,Uranium%20series%29.PNG) [Access on: 12.10.2020].
- [48] F. Fränkle and KATRIN collaboratio. “Background processes in the KATRIN main spectrometer ”. In: *Journal of Physics Conference Series* 888 012070 (2017).
- [49] J. Schwarz. *Background Investigation at Increased Argon Pressure*. 2013 KATRIN Collaboration Meeting, Session D1.
- [50] J.Schwarz. “The Detector System of the KATRIN Experiment Implementation and First Measurements with the Spectrometer”. PhD thesis. Karlsruher Institut für Technologie (KIT), 2014.

- [51] U. Even. “ Decay dynamics of high Rydberg states in atoms and molecules ”. In: (1997).
- [52] G. Higgins. “ A Single Trapped Rydberg Ion ”. PhD thesis. Stockholm University, 2019.
- [53] A. Burgess. “ Tables of hydrogenic photoionization cross-sections and recombination coefficients ”. In: *Memoirs of the Royal Astronomical Society* 69 (1965).
- [54] I. Beterov et al. “ Ionization of Rydberg atoms by blackbodyradiation ”. In: *New Journal of Physics* (2009).
- [55] O. Auciello and S. Dzioba R. Kelly. “ On the kinetic energies of sputtered excited particles, I. Atoms sputtered from Li, LiF, and NaCl ”. In: *Radiation Effects* (1980). DOI: 10.1080/00337578008208435.
- [56] H. Hinz et al. *Background of the KATRIN Experiment*. [Online]. Available: <https://nusoft.fnal.gov/nova/nu2020postersession/pdf/posterPDF-125.pdf> [Access on: 08.11.2020].
- [57] R. Behrisch W. Eckstein. *Sputtering by Particle Bombardment*. Springer-Verlag Berlin Heidelberg, 2007.
- [58] P. Sigmund. “ Sputtering by ion bombardment theoretical concepts ”. In: *Topics in Applied Physics, vol 47* (1981).
- [59] D. Rosenberg G. Wehner. “ Sputtering Yields for Low Energy He<sup>+</sup>-, Kr<sup>+</sup>-, and Xe<sup>+</sup>-Ion Bombardment ”. In: *JOURNAL OF APPLIED PHYSICS VOLUME 33, NUMBER 5* (1961).
- [60] P. Sigmund. “ Theory of sputtering. I. Sputtering yield of amorphous and polycrystalline targets ”. In: *Physical Review, Volume 184 Number 2* (1981).
- [61] Geant4 Collaboration. *Book For Application Developers Release 10.6*. 2019.
- [62] J. Ziegler, J. Biersack, and M. Ziegler. *SRIM - The Stopping and Range of Ions in Matter*. SRIM, 2008.
- [63] S. Agostinelli et al. “ Geant4 — a simulation toolkit ”. In: *Nuclear Instruments and Methods in Physics Research Section A: Accelerators, Spectrometers, Detectors and Associated Equipment* (2003).
- [64] G Bellini et al. “ Cosmogenic Backgrounds in Borexino at 3800 m water-equivalent depth ”. In: *Journal of Cosmology and Astroparticle Physics* 2013.08 (Aug. 2013), pp. 049–049. ISSN: 1475-7516. DOI: 10.1088/1475-7516/2013/08/049. URL: <http://dx.doi.org/10.1088/1475-7516/2013/08/049>.
- [65] M. Kuzniak et al. “ Surface roughness interpretation of 730 kg days CRESST-II results ”. In: *Astroparticle Physics* 36 (2012) 77–82 (2012).
- [66] J. Chapman et al. *Fast simulation methods in ATLAS: from classical to generative models*. Tech. rep. ATL-SOFT-PROC-2020-035. Geneva: CERN, Oct. 2020. URL: <https://cds.cern.ch/record/2740905>.
- [67] Geant4 Collaboration. *Reference Physics Lists*. [Online]. Available: <https://geant4.web.cern.ch/node/155> [Access on: 12.10.2020].

- 
- [68] E. Luiken. *Möglichkeiten zur Optimierung von Oberflächen durch Elektropolieren*. [Online]. Available: [https://www.ptb.de/cms/ptb/fachabteilungen/abt5/nachrichten-abt-5/forschungsnachricht-aktuell.html?tx\\_news\\_pi1%5Bnews%5D=746&tx\\_news\\_pi1%5Bcontroller%5D=News&tx\\_news\\_pi1%5Baction%5D=detail&tx\\_news\\_pi1%5Bday%5D=1&tx\\_news\\_pi1%5Bmonth%5D=12&tx\\_news\\_pi1%5Byear%5D=2010&cHash=edb02201c0d21041053a27559dce05c4](https://www.ptb.de/cms/ptb/fachabteilungen/abt5/nachrichten-abt-5/forschungsnachricht-aktuell.html?tx_news_pi1%5Bnews%5D=746&tx_news_pi1%5Bcontroller%5D=News&tx_news_pi1%5Baction%5D=detail&tx_news_pi1%5Bday%5D=1&tx_news_pi1%5Bmonth%5D=12&tx_news_pi1%5Byear%5D=2010&cHash=edb02201c0d21041053a27559dce05c4) [Access on: 12.10.2020].
- [69] M. Mendenhal R. Weller. “An algorithm for computing screened Coulomb scattering in GEANT4”. In: *Nuclear Instruments and Methods in Physics Research B 227 (2005) 420–430* (2004).
- [70] M. Mendenhal R. Weller. “Algorithms for the rapid computation of classical cross sections for screened Coulomb collisions”. In: *Nuclear Instruments and Methods in Physics Research B58 (1991) 11-17* (1991).
- [71] Basunia M. “Nuclear Data Sheets for A = 210”. In: *Nuclear Data Sheets 121*, p. 561–694 (2014).
- [72] M. Arenz et al. “Commissioning of the vacuum system of the KATRIN Main Spectrometer”. In: *Journal of Instrumentation* (2016).
- [73] Spektrum Akademischer Verlag. *Bindungslänge*. [Online]. Available: <https://www.spektrum.de/lexikon/physik/bindungslaenge/1612> [Access on: 13.10.2020].
- [74] “Appendix 7 A7. Mean Excitation Energy”. In: *Journal of the International Commission on Radiation Units and Measurements* (2016). ISSN: 1473-6691. DOI: 10.1093/jicru/os9.1.36. eprint: <https://academic.oup.com/jicru/article-pdf/os9/1/36/9587765/jicruos9-0036.pdf>.
- [75] J. Yoon et al. “Cross Sections for Electron Collisions with Hydrogen Molecules”. In: *Journal of Physical and Chemical Reference* (2008). DOI: <https://doi.org/10.1063/1.2838023>.
- [76] Y. Itikawa and N. Mason. “Cross Sections for Electron Collisions with Water Molecules”. In: *Journal of Physical and Chemical Reference Data* (2005). DOI: 10.1063/1.1799251.
- [77] A. Gupta K. Baluja. “Total cross-sections for electron scattering from iron at 10–5000 eV using a model optical potential”. In: *Zeitschrift für Physik D Atoms, Molecules and Clusters volume 31* (1994).
- [78] L. Kippenbrock. “Investigation of Background from the Inter-Spectrometer Penning Trap and Secondary Electron Emission in the KATRIN Experiment”. PhD thesis. University of Washington, 2019.
- [79] KATRIN Collaboration. *Kassiopeia*. [Online]. Available: <https://ikp-katrin-wiki.ikp.kit.edu/katrin/index.php/Kassiopeia> [Access on: 14.11.2020].
- [80] S. Mertens. “Study of Background Processes in the Electrostatic Spectrometers of the KATRIN Experiment”. PhD thesis. Karlsruher Institut für Technologie (KIT), 2012.
- [81] F. Fränkle et al. “Tritium background in the KATRIN spectrometers”. In: *intern* (2020).

- [82] G.Vandoni. *THE BASIS of VACUUM*, CERN. [Online]. Available: <https://indico.cern.ch/event/264020/attachments/467855/648232/CERN-Basic-Vacuum-2012-lecture.pdf> [Access on: 02.11.2020].
- [83] A. Kähm. “Investigation of background processes caused by stored electrons”. MA thesis. Karlsruher Institut für Technologie (KIT), 2020.
- [84] A. Lokhov. *Shifted analyzing plane configuration for the neutrino mass measurements*. 39th KATRIN Collaboration Meeting: [Online]. Available: [https://indico.scc.kit.edu/event/765/contributions/7581/attachments/3696/5444/CM39\\_Lokhov\\_SAP\\_final.pdf](https://indico.scc.kit.edu/event/765/contributions/7581/attachments/3696/5444/CM39_Lokhov_SAP_final.pdf) [Access on: 22.11.2020].
- [85] E. Ellinger. *Probing background reduction in KATRIN by induced de-excitation of Rydberg atoms with THz radiation*. [Online]. Available: <https://nusoft.fnal.gov/nova/nu2020postersession/pdf/posterPDF-361.pdf> [Access on: 23.11.2020].
- [86] KATRIN internal. *Nu Mass 2*. [Online]. Available: [https://ikp-katrin-wiki.ikp.kit.edu/katrin/index.php/Nu\\_Mass\\_2](https://ikp-katrin-wiki.ikp.kit.edu/katrin/index.php/Nu_Mass_2) [Access on: 04.11.2020].

# A. Appendix

## A.1. Stainless steel composition in Geant4

Material: G4\_STAINLESS-STEEL density: 8.000 g/cm<sup>3</sup> RadL: 1.738 cm Nucl.

Int. Length: 16.678 cm I<sub>mean</sub>: 282.977 eV temp.: 293.15 K pressure: 1.00 atm

—> Element: Fe (Fe) Z = 26.0 N = 56 A = 55.845 g/mole  
—> Isotope: Fe54 Z = 26 N = 54 A = 53.94 g/mole abundance: 5.84 %  
—> Isotope: Fe56 Z = 26 N = 56 A = 55.93 g/mole abundance: 91.754 %  
—> Isotope: Fe57 Z = 26 N = 57 A = 56.94 g/mole abundance: 2.119 %  
—> Isotope: Fe58 Z = 26 N = 58 A = 57.93 g/mole abundance: 0.282 %  
ElmMassFraction: 74.62 % ElmAbundance 74.00 %

—> Element: Cr (Cr) Z = 24.0 N = 52 A = 51.996 g/mole  
—> Isotope: Cr50 Z = 24 N = 50 A = 49.95 g/mole abundance: 4.345 %  
—> Isotope: Cr52 Z = 24 N = 52 A = 51.94 g/mole abundance: 83.789 %  
—> Isotope: Cr53 Z = 24 N = 53 A = 52.94 g/mole abundance: 9.501 %  
—> Isotope: Cr54 Z = 24 N = 54 A = 53.94 g/mole abundance: 2.365 %  
ElmMassFraction: 16.90 % ElmAbundance 18.00 %

—> Element: Ni (Ni) Z = 28.0 N = 59 A = 58.693 g/mole  
—> Isotope: Ni58 Z = 28 N = 58 A = 57.94 g/mole abundance: 68.077 %  
—> Isotope: Ni60 Z = 28 N = 60 A = 59.93 g/mole abundance: 26.223 %  
—> Isotope: Ni61 Z = 28 N = 61 A = 60.93 g/mole abundance: 1.140 %  
—> Isotope: Ni62 Z = 28 N = 62 A = 61.93 g/mole abundance: 3.635 %  
—> Isotope: Ni64 Z = 28 N = 64 A = 63.93 g/mole abundance: 0.926 %  
ElmMassFraction: 8.48 % ElmAbundance 8.00 %

## A.2. Penetration depth and variance along the decay chain

Table A.1.: Change of penetration depth and smearing out during decay chain. Also the number of particle decreases constantly. In this data set smooth surface condition is used.

	mean	variance	number of particles
$^{218}\text{Po}$	8.42	5.66	1 700 000
$^{214}\text{Pb}$	13.69	9.13	1 265 682
$^{214}\text{Po}$	13.73	9.11	1 261 817
$^{210}\text{Pb}$	19.00	12.40	1 021 047

## A.3. Sputtering Simulation results

All figures in this section follows these boundary conditions:

Surface layer consist of 0.3 mono layer of hydrogen

Statistic smooth surface condition: 1 500 000

Statistic rough surface condition: 200 000

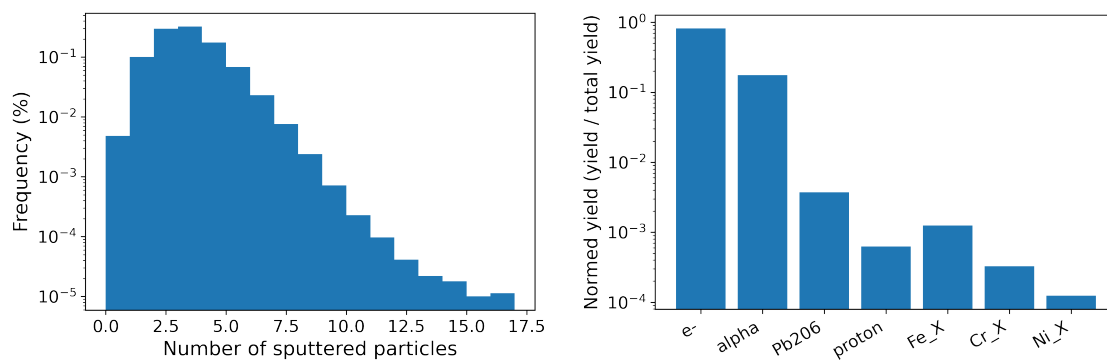


Figure A.1.: Smooth surface condition - Left: Total Sputter yield. Right: Normalised sputter yield broken down by particle type.

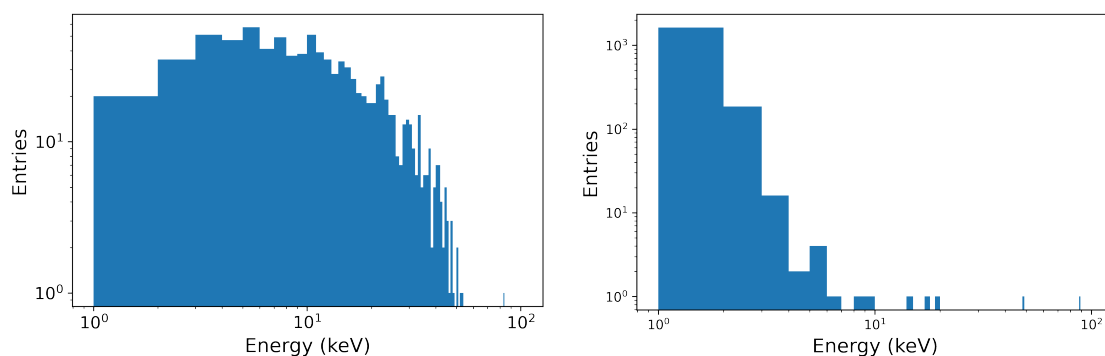


Figure A.2.: Smooth surface condition - Left: Energy distribution of all Cr isotopes. Right: Energy distribution of hydrogen

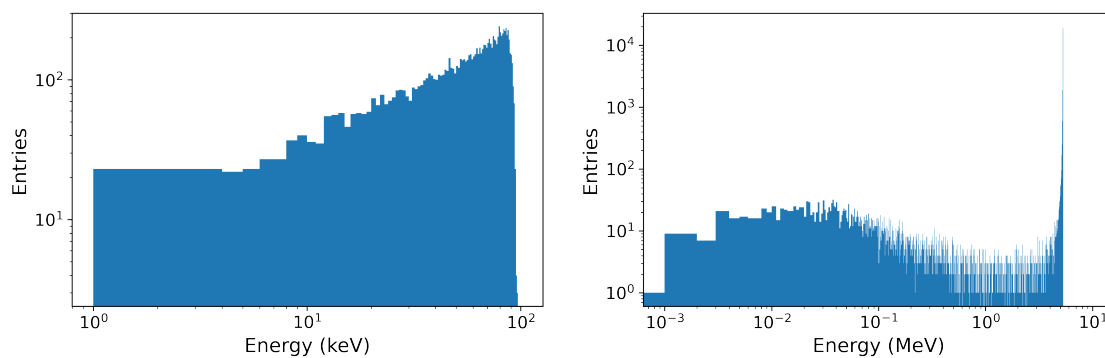


Figure A.3.: Smooth surface condition - Left: Energy distribution of  $^{206}\text{Pb}$ . Right: Energy distribution of alpha

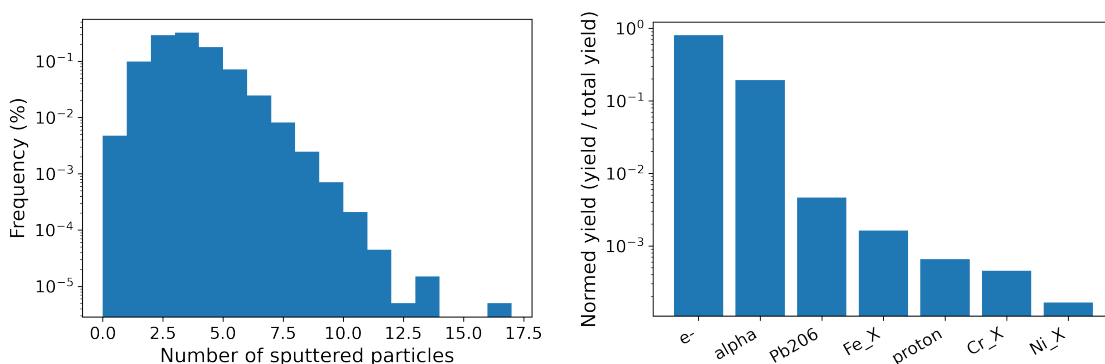


Figure A.4.: Rough surface condition - Left: Total Sputter yield. Right: Normalised sputter yield broken down by particle type.

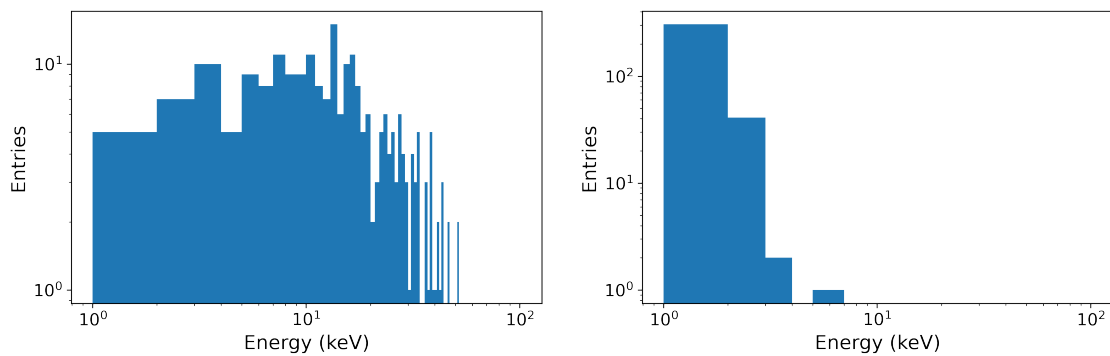


Figure A.5.: Rough surface condition - Left: Energy distribution of all Cr isotopes. Right: Energy distribution of hydrogen

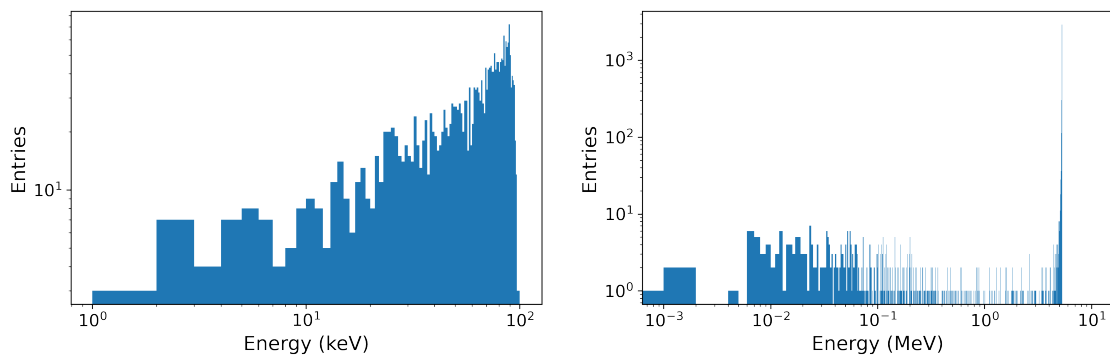


Figure A.6.: Rough surface condition - Left: Energy distribution of  $^{206}\text{Pb}$ . Right: Energy distribution of alpha

## A.4. Excluded pixels and run numbers

Table A.2.: Enumeration of the excluded detector pixels. For analysis purposes it is necessary to exclude pixels which are shadowed or defect [86]. Normalisation to effective pixel number in this context means the multiplication of the events by the factor  $\frac{\text{total number of ring pixel}}{\text{number of used ring pixel}}$ .

Reason	Excluded pixels	Total = 31 pixels
Wafer	97 98 110 111 121 122	6 pixels
FBM	100	1 pixel
Alignment	112 113 123 124 125 126 127 128 129 130 134 135 136 137 138 139 140 141 142 143 144 145 146 147	24 pixels

Table A.3.: List of run numbers for different data sets.

KNM2_Period1a	KNM2_Period1b	KNM2_Period2	KNM2_Period3	KNM3a
56160-56174	56278 - 56282	56560 - 56566	57015 - 57020	62784 - 62790
56176-56184	56284 - 56294	56575 - 56595	57022 - 57026	62794 - 62802
56186-56196	56301 - 56317	56598 - 56613	57035 - 57036	62807 - 62814
56268-56272	56319 - 56330	56621 - 56629	57038 - 57062	62819 - 62828
56274-56277	56333 - 56338	56636 - 56636	57068 - 57096	62835 - 62837
	56341 - 56370	56639 - 56648	57103 - 57111	62846 - 62862
	56379 - 56407	56654 - 56664	57120 - 57136	62867 - 62875
	56409 - 56409	56669 - 56674		62885 - 62890
	56412 - 56418	56684 - 56685		62902 - 62907
	56472 - 56479	56688 - 56693		62915 - 62923
				62929 - 62957

Table A.4.: List of run numbers for different data sets.

KNM3b	KNM4	TritiumContaminationI	TritiumContaminationII
63308 - 63315	65496 - 65520	58607 - 58622	58506 - 58509
63318 - 63319	65544 - 65546	58626 - 58638	58521 - 58553
63325 - 63331	65546 - 65578	58645 - 58673	58562 - 58567
63337 - 63345	65580 - 65594	58676 - 58679	58569 - 58579
63363 - 63370	65596 - 65596	58681 - 58681	
63376 - 63402	65596 - 65617	58683 - 58683	
63404 - 63404	65621 - 65626	58685 - 58688	
63406 - 63414	65631 - 65669	58690 - 58701	
63418 - 63423	65677 - 65707	58703 - 58710	
63425 - 63426	65709 - 65721	58712 - 58712	
63428 - 63436	65725 - 65730		
63438 - 63447			

## A.5. Background rates over time per ring

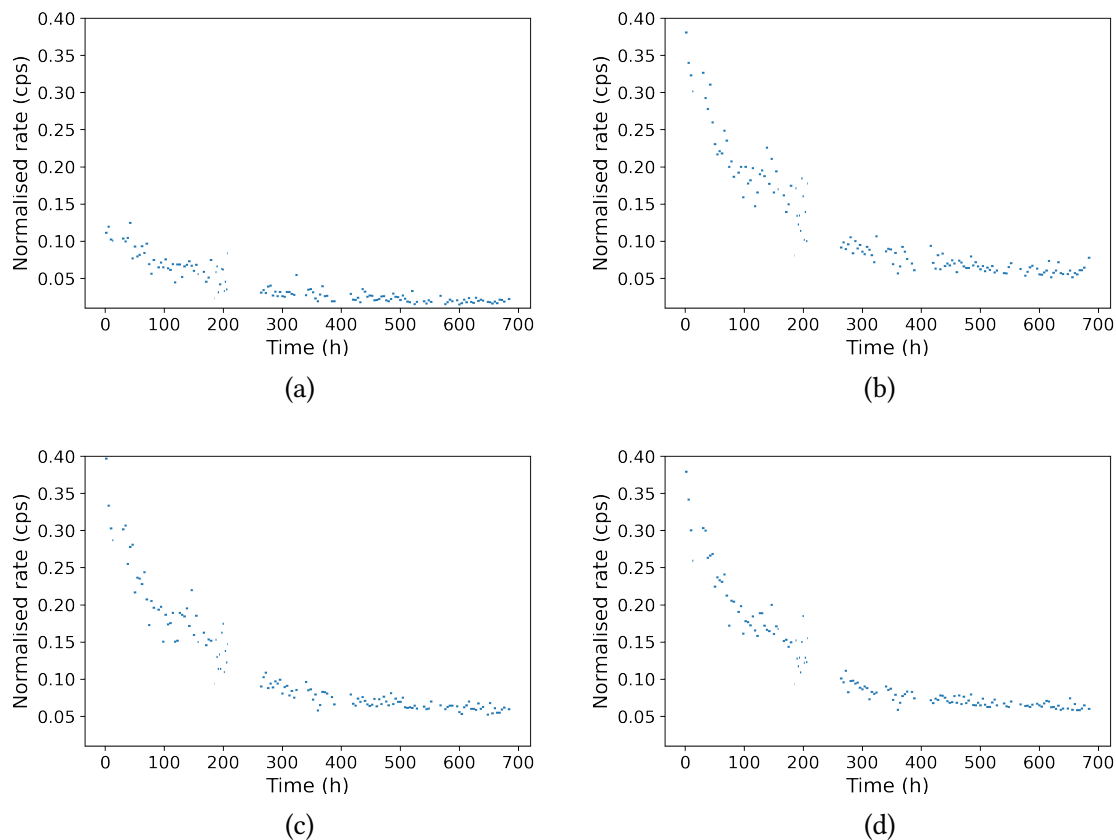


Figure A.7.: Background Rates over time per ring. Each data point represent the background rate of one TritiumContamination run, see table A.4. Normalised to effective pixel number, see table A.2. **(a)**: Ring number 1 **(b)**: Ring number 2 **(c)**: Ring number 3 **(d)**: Ring number 4

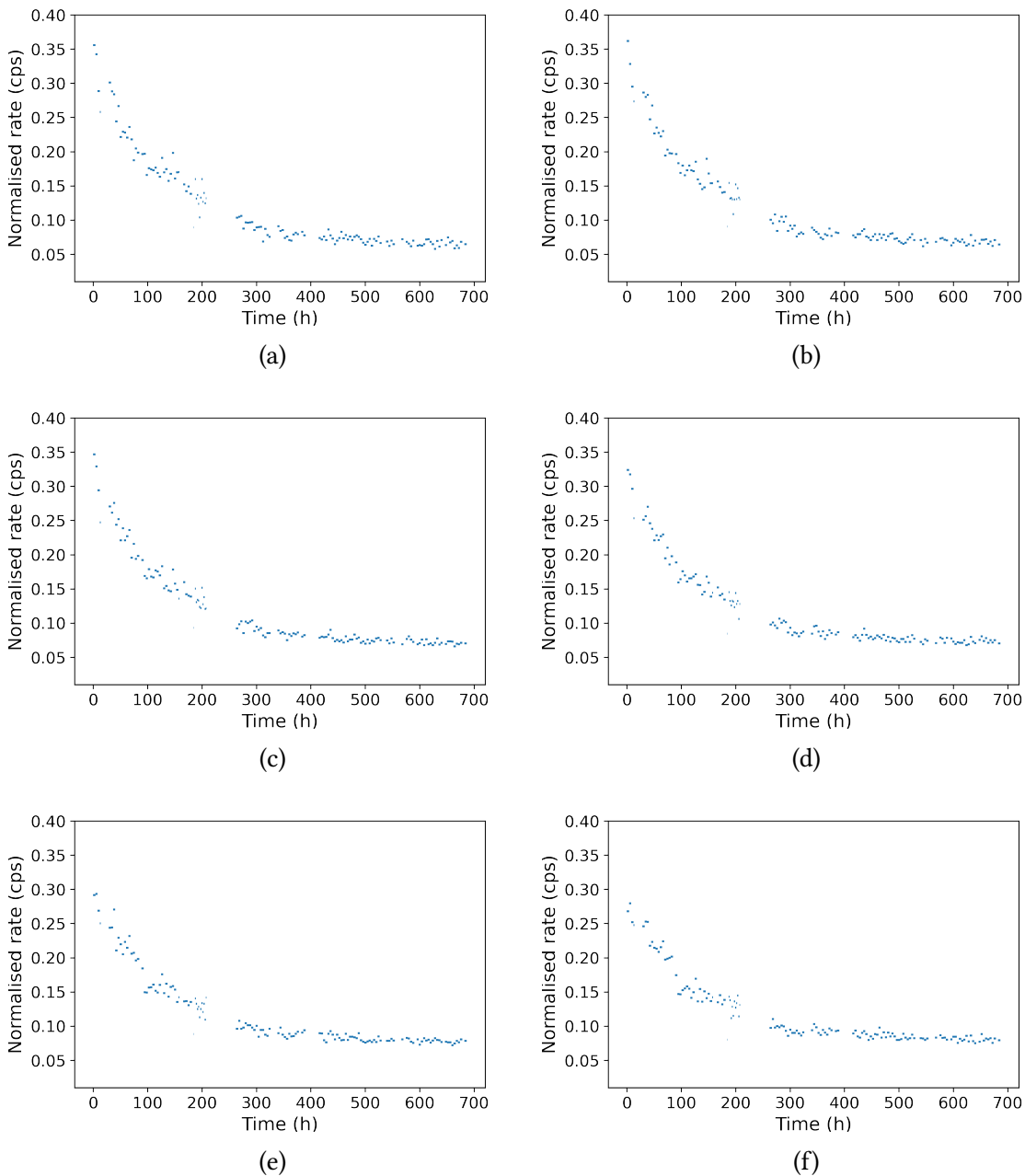


Figure A.8.: Background Rates over time per ring. Each data point represent the background rate of one TritiumContamination run, see table A.4. Normalised to effective pixel number, see table A.2. **(a)**: Ring number 5 **(b)**: Ring number 6 **(c)**: Ring number 7 **(d)**: Ring number 8 **(e)**: Ring number 9 **(f)**: Ring number 10

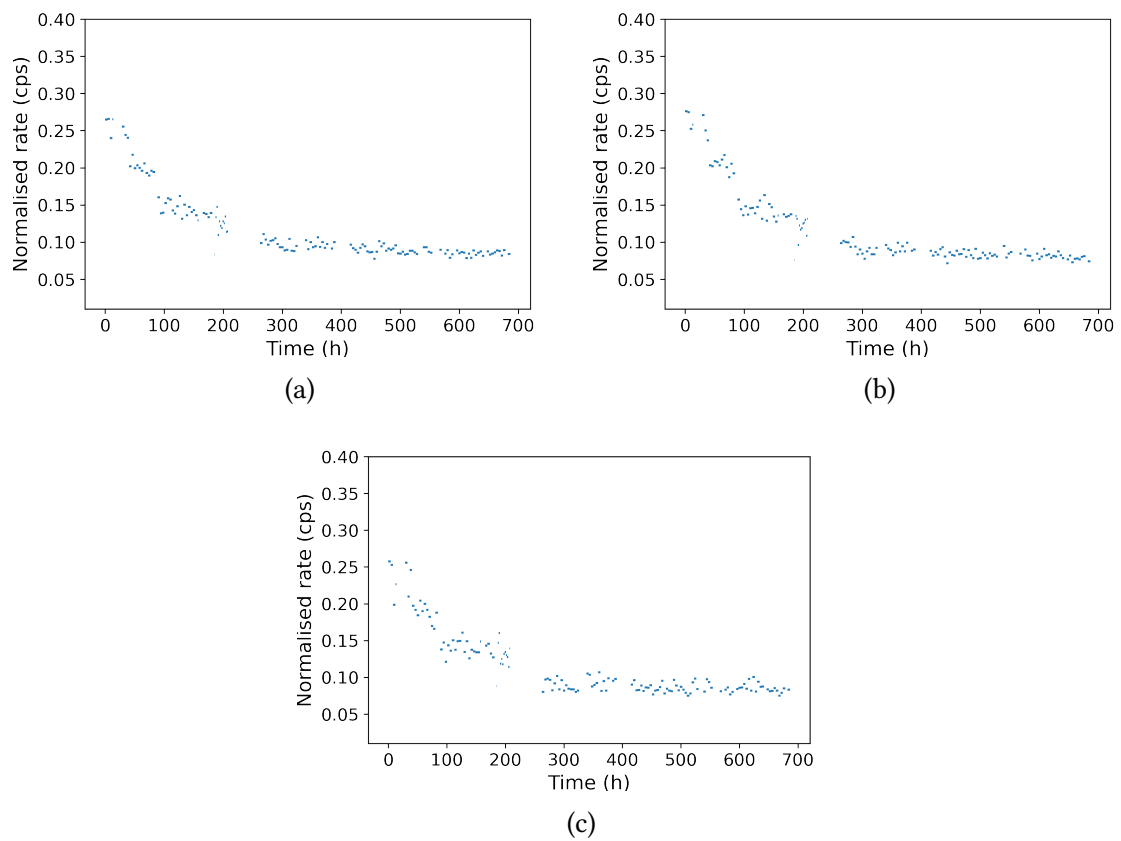


Figure A.9.: Background Rates over time per ring. Each data point represent the background rate of one TritiumContamination run, see table A.4. Normalised to effective pixel number, see table A.2. **(a)**: Ring number 11 **(b)**: Ring number 12 **(c)**: Ring number 13